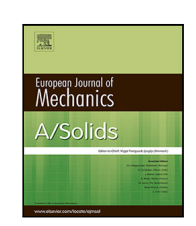
# RTICLE IN PRE

European Journal of Mechanics / A Solids xxx (xxxx) xxx

Contents lists available at ScienceDirect

# European Journal of Mechanics / A Solids

journal homepage: www.elsevier.com/locate/ejmsol



# An analysis of failure in shear versus tension

R. Vigneshwaran, A.A. Benzerga

Department of Aerospace Engineering, Texas A&M University, College Station, TX 77843, United States of America

## ARTICLE INFO

## Keywords: Porous material Ductile fracture Void growth Unhomogeneous yielding

### ABSTRACT

The micromechanics of ductile failure is revisited using the voided cell model. Emphasis is laid on comparing shearing stress states with axisymmetric states. The unit cell is subjected to proportional loading and fully periodic boundary conditions. The progression of elastic unloading in the unit cell is analyzed, leading to a definition of unhomogeneous yielding. Overall strain localization is determined by evaluating "on the fly" the tangent operator using a perturbation method. The connection between unhomogeneous yielding and strain localization is thus thoroughly investigated. Other potentially critical strain measures are introduced and their relevance to failure by void coalescence or strain localization is discussed. The effects of initial porosity and strain hardening in modulating the relative ductility under tension versus shear are further examined.

### 1. Introduction

The effect of stress state on the ductility of materials is a subject of long-standing interest. The trend for axisymmetric loadings has long been established based on experiments (Hancock and Mackenzie, 1976), continuum damage models (Gurson, 1977; Needleman and Tvergaard, 1984) and direct numerical simulations (Koplik and Needleman, 1988): the ductility decreases drastically with increasing hydrostatic tension. For non-axisymmetric states, the torsion experiments of Johnson et al. (1983) have long suggested that the ductility in shear is much larger than that in (axisymmetric) tension. Recent experiments confirm this trend for a broader range of shearing states (Haltom et al., 2013). Other experiments, however, have suggested otherwise, e.g. Bao and Wierzbicki (2004), Barsoum and Faleskog (2007a). Phenomenological failure models have subsequently been developed, which predict a lower ductility for shearing states in comparison with axisymmetric states (Nahshon and Hutchinson, 2008; Xue, 2008; Bai and Wierzbicki, 2010). Later, direct numerical simulations that employ the voided cell model pioneered by Tvergaard (1981, 1982b,a) provided what seems like a solid basis to this trend, by exploring the effect of the third stress invariant, e.g. Barsoum and Faleskog (2007b, 2011), Dunand and Mohr (2014), Vishwakarma and Keralavarma (2019). Thus, the body of available cell model analyses is consistent with the prevailing interpretation of the experiments of Bao and Wierzbicki (2004), Barsoum and Faleskog (2007a) but keeps the interpretation of the experiments of Johnson et al. (1983), Haltom et al. (2013) wide open.

The aim of this paper is to investigate the relative ductility under shearing versus axisymmetric states and contribute toward reconciling apparently conflicting experiments. To this end, the unit cell model is employed under fully periodic boundary conditions. Departure from the cell model literature is two-fold. First, we explore the effect of initial porosity content in mediating possible transitions from shearing states being "less ductile" than axisymmetric states to their being "more ductile" than axisymmetric states. Second, since any such comparison requires a definition of ductility, we characterize for the first time the spatial distribution of elastic unloading in the cell model. In so doing, we introduce the concept of unhomogeneous yielding as a mode of macroscopically nonuniform deformation that corresponds to a welldefined critical percolation state in the progression of elastic unloading. This concept is consistent with recent developments in porous material plasticity (Benzerga, 2023). The notion of unhomogeneous yielding is conceptually useful because (i) its initiation corresponds exactly to what has been referred to in the literature as the "onset of void coalescence" for axisymmetric stress states (Pardoen and Hutchinson, 2000; Benzerga, 2002); and (ii) it applies to more general states of loading, even though it is not meant to define a measure of ductility.

Another issue that has received wide attention is whether the onset of void coalescence occurs before or after macroscopic strain localization. If well posed, not only does the question have theoretical significance, e.g. in developing failure models (Morin et al., 2016; Keralavarma, 2017; Torki et al., 2021; Khan et al., 2023), but also practical value since its resolution may provide the most suitable ductility measure needed in settling the main question of the paper.

Under axisymmetric tension, the onset of void coalescence in the cell model manifests as a shift to a uniaxial straining mode associated with necking of the intervoid ligament (Koplik and Needleman, 1988). Under shear loading, the situation is more complex, as studied

E-mail address: benzerga@tamu.edu (A.A. Benzerga).

https://doi.org/10.1016/j.euromechsol.2023.105074

Received 1 May 2023; Received in revised form 7 July 2023; Accepted 7 July 2023 Available online 11 July 2023

0997-7538/© 2023 Elsevier Masson SAS. All rights reserved.

Corresponding author.

by Tyergaard (2008, 2009), Leblond and Mottet (2008), Scheyvaerts et al. (2011). Nielsen et al. (2012) and others. To quantify ductility, Barsoum and Faleskog (2007b) first introduced an ad hoc strain concentration measure in the cell. The measure has been adopted in many subsequent cell analyses as surrogate to strain localization in the sense of Rice (1976). There is confusion about what the measure truly means. For under axisymmetric tension, the strain concentration criterion of Barsoum and Faleskog (2007b) does correspond to the onset of void coalescence. Thus, its use as a surrogate localization criterion assumes that, at least for tension, the onset of void coalescence and strain localization coincide. However, when Tekoğlu et al. (2015) investigated the said competition between coalescence and localization, they introduced a new ad hoc strain concentration measure for the onset of void coalescence. Both the measure and the meaning of the "onset of void coalescence" for non-axisymmetric stress states are problematic: the conclusions drawn by Tekoğlu et al. (2015) are thus questionable.

Several works have since revisited the competition between void coalescence and strain localization. None of these employed the strain concentration measure of Tekoğlu et al. (2015) to define the onset of void coalescence. Instead, most cell model analyses have settled on using an energy criterion, first introduced by Wong and Guo (2015), for defining the onset of void coalescence. Cadet et al. (2021) used a kinematic criterion as an alternative. Both criteria have indubitable validity under axisymmetric loadings. For more general states, however, their physical meaning has not been demonstrated.

Computational methods for probing directly strain localization in cell model analyses have been around for quite some time (Miehe et al., 2002; Miehe, 2003; Temizer and Wriggers, 2008). Yet, only recently have these methods been applied to porous cells (Zhu et al., 2020; Cadet et al., 2022). Each method aims at evaluating the acoustic tensor entering the localization condition of Rice (1976). Miehe et al. (2002) introduced a method whereby the overall tangent modulus is additively decomposed into an average term and a fluctuation term. Then, Miehe (2003) developed a sophisticated technique whereby the overall tangent modulus is obtained by condensing the finite element global stiffness matrix. Later, Temizer and Wriggers (2008) introduced a simpler, albeit computationally expensive, method based on perturbing the overall deformation gradient to obtain the overall tangent modulus via the forward difference of the overall nominal stress. Here, following along the lines of Zhu et al. (2020), Cadet et al. (2022) we employ one of these methods to directly probe strain localization in the porous cell. However, we go beyond these works in that we also critically analyze the energy criterion of Wong and Guo (2015), which has been used for the onset of void coalescence in recent years.

The article is organized as follows. Section 2 provides the methods used to perform unit cell calculations and post-process the results. In particular, Section 2.3 gathers all criteria used to date in discussing void coalescence or strain localization in the cell model literature. Results in Section 3 are organized so as to address the main question in Section 3.1 and a critical analysis of all criteria in Section 3.2. The main finding is reported in Fig. 9. General implications and open issues are discussed in Section 4.

## 2. Methods

## 2.1. Problem formulation

Three-dimensional finite deformation calculations are carried out using the voided cell model pioneered by Tvergaard (1982b). The computational procedure follows the general formulation of Barsoum and Faleskog (2007b), as revisited by others, e.g. Dunand and Mohr (2014), Tekoglu (2014), Zhu et al. (2018), Tekoglu and Koçhan (2022), Dæhli et al. (2022) with some amendments. The tetragonal unit cell is reported to a set of Cartesian coordinates with basis ( $\mathbf{e}_1$ ,  $\mathbf{e}_2$ ,  $\mathbf{e}_3$ ), Fig. 1a. It has initial dimensions  $2A_0$ ,  $2B_0$ ,  $2A_0$ . The cell contains a central,

initially spherical void with radius  $r_0$ . The initial void volume fraction (or porosity) is thus  $f_0=(\pi r_0^3)/(6A_0B_0^2)$ .

The elastoplastic matrix is modeled using a standard finite strain  $J_2$  flow theory, assuming additive decomposition of the rate of deformation  $\mathbf{d} = \mathbf{d}^c + \mathbf{d}^p$  and isotropic hypoelasticity (Young's modulus E and Poisson's ratio  $\nu$ ). The yield criterion and flow rule read:

$$\phi(\sigma) = \sigma_{\rm eq} - \sigma_{\rm v} \le 0 \tag{1}$$

$$\mathbf{d}^{\mathbf{p}} = \frac{3}{2} \frac{d_{\mathbf{eq}}}{\sigma_{\mathbf{eq}}} \sigma' \tag{2}$$

where  $\sigma_{\rm eq}$  is the von Mises effective stress,  $\sigma_{\rm y}$  the current yield stress and  $d_{\rm eq}$  the effective strain rate, identified with the plastic multiplier. The prime stands for the deviator. Voce-type laws are more physical, e.g. Vigneshwaran and Benzerga (2023), but a power law isotropic hardening is used here for convenience:

$$\sigma_{y} = \sigma_{0} \left( 1 + \frac{\bar{\epsilon}}{\epsilon_{0}} \right)^{N} \tag{3}$$

where  $\bar{e}=\int d_{\rm eq}\,{\rm d}t$  is the equivalent plastic strain and  $\sigma_0,~\epsilon_0,~N$  are parameters,  $\sigma_0$  being the initial yield stress and N the hardening exponent.

Fully periodic boundary conditions are imposed on the unit cell. Relative displacements of points in periodic correspondence are written as:

$$\begin{aligned} \mathbf{u}(A_0, x_2, x_3) - \mathbf{u}(-A_0, x_2, x_3) &= 2A_0(\mathbf{F} - \mathbf{I})\mathbf{e}_1 \\ \mathbf{u}(x_1, B_0, x_3) - \mathbf{u}(x_1, -B_0, x_3) &= 2B_0(\mathbf{F} - \mathbf{I})\mathbf{e}_2 \\ \mathbf{u}(x_1, x_2, A_0) - \mathbf{u}(x_1, x_2, -A_0) &= 2A_0(\mathbf{F} - \mathbf{I})\mathbf{e}_3 \end{aligned} \tag{4}$$

where  $\mathbf{F}$  is the overall deformation gradient, taken as the volume average of its microscopic counterpart, and  $x_i$  denote coordinates in the initial, undeformed configuration.

The overall stress is defined as the volume average over the unit cell of the microscopic (Cauchy) stress:

$$\Sigma = \frac{1}{\Omega} \int_{\Omega} \sigma \, \mathrm{d}\Omega \tag{5}$$

where  $\Omega = 8ABC$  is the current cell volume, determined in terms of the dimensions A, B, C of an equivalent parallelepiped having the same volume as the deformed unit cell (Zhu et al., 2018). The Eulerian (logarithmic) strain tensor, E, is defined as

$$\mathbf{E} = \ln \mathbf{V} \qquad \text{with} \qquad \mathbf{V}^2 = \mathbf{F} \mathbf{F}^{\mathrm{T}} \tag{6}$$

where V stands for the (overall) left stretch tensor. The overall equivalent stress,  $\Sigma_{\rm eq}$ , and equivalent strain,  $E_{\rm eq}$ , are then defined as:

$$\Sigma_{\text{eq}} = \sqrt{\frac{3}{2}\Sigma' : \Sigma'}, \qquad E_{\text{eq}} = \sqrt{\frac{2}{3}\mathbf{E}' : \mathbf{E}'}$$
 (7)

Here, the unit cell is subjected to one shear stress,  $\Sigma_{12}$ , and three normal stresses,  $\Sigma_{11}$ ,  $\Sigma_{22}$ ,  $\Sigma_{33} = \Sigma_{11}$ . Hence, the non-zero components of E can be written in terms of the deformation gradient components as follows (Wong and Guo, 2015)

$$E_{11} = \frac{1}{2} \ln \left( F_{11} F_{22} \right) + \frac{1}{2} \frac{F_{12}^2 + F_{11}^2 - F_{22}^2}{\alpha \beta} \ln \left( \frac{\alpha + \beta}{\alpha - \beta} \right)$$
 (8)

$$E_{22} = \frac{1}{2} \ln \left( F_{11} F_{22} \right) - \frac{1}{2} \frac{F_{12}^2 + F_{11}^2 - F_{22}^2}{\alpha \beta} \ln \left( \frac{\alpha + \beta}{\alpha - \beta} \right) \tag{9}$$

$$E_{33} = \ln F_{33} \tag{10}$$

$$E_{12} = \frac{F_{12}F_{22}}{\alpha\beta} \ln\left(\frac{\alpha+\beta}{\alpha-\beta}\right) \tag{11}$$

where

$$\alpha = \sqrt{F_{12}^2 + (F_{11} + F_{22})^2} \quad \beta = \sqrt{F_{12}^2 + (F_{11} - F_{22})^2}$$
 (12)

Throughout, proportional stressing is considered using two stress ratios:

$$\rho = \frac{\Sigma_{11}}{\Sigma_{22}} = \frac{\Sigma_{33}}{\Sigma_{22}}, \qquad \kappa = \frac{\Sigma_{12}}{\Sigma_{22}} \tag{13}$$

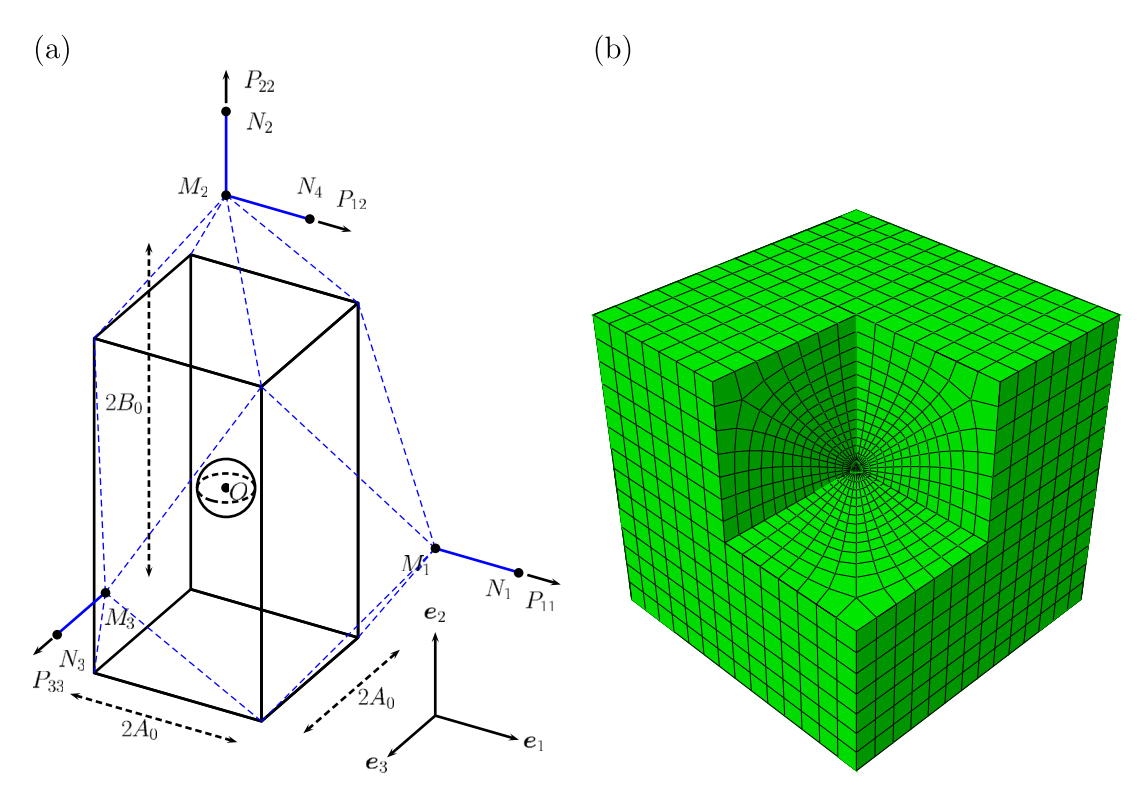


Fig. 1. (a) Geometry of the unit cell with a void in the middle, master nodes  $(M_1, M_2, M_3)$  and dummy nodes  $(N_1, N_2, N_3, N_4)$  for the procedure of imposing proportional loading conditions. (b) Finite element mesh of the full 3D unit cell.

The overall stress triaxiality ratio,  $T = \Sigma_{\rm eq}/\Sigma_{\rm m}$ , and the Lode parameter,  $L = \left(2\Sigma_2 - \Sigma_1 - \Sigma_3\right)/\left(\Sigma_3 - \Sigma_1\right)$  are related to the stress ratios by:

$$T = \frac{(1+2\rho)\operatorname{sgn}(\Sigma_{22})}{3\sqrt{(1-\rho)^2 + 3\kappa^2}} \qquad L = -\frac{(1-\rho)\operatorname{sgn}(\Sigma_{22})}{\sqrt{(1-\rho)^2 + 4\kappa^2}}$$
(14)

Above,  $\Sigma_{\rm eq}$  is given by Eq. (7)<sub>1</sub>,  $\Sigma_{\rm m}=\frac{1}{3}{\rm tr}\,\Sigma$ , and the  $\Sigma_i$ 's denote principal stresses ( $\Sigma_1\leq \Sigma_2\leq \Sigma_3$ ).

# 2.2. Implementation

All calculations are carried out using the finite element software ABAQUS/Standard 2021. Imposing the periodic boundary conditions, Eq. (4), requires corresponding discretization of opposite faces. Moreover, to impose the periodic boundary conditions, master nodes  $M_1$ ,  $M_2$ ,  $M_3$  are defined for each pair of opposite faces (Fig. 1) such that:

$$\mathbf{u}^{M_1} = A_0(\mathbf{F} - \mathbf{I})\mathbf{e}_1, \quad \mathbf{u}^{M_2} = B_0(\mathbf{F} - \mathbf{I})\mathbf{e}_2, \quad \mathbf{u}^{M_3} = A_0(\mathbf{F} - \mathbf{I})\mathbf{e}_3$$
 (15)

On account of this, the periodic boundary conditions, Eq. (4), are rewritten as

$$\mathbf{u}(A_0, x_2, x_3) - \mathbf{u}(-A_0, x_2, x_3) = 2\mathbf{u}^{M_1}$$

$$\mathbf{u}(x_1, B_0, x_3) - \mathbf{u}(x_1, -B_0, x_3) = 2\mathbf{u}^{M_2}$$

$$\mathbf{u}(x_1, x_2, A_0) - \mathbf{u}(x_1, x_2, -A_0) = 2\mathbf{u}^{M_3}$$
(16)

where, given the non-zero components of **F**, the relevant terms are the three normal displacements  $u_1^{M_1} \equiv u_1, u_2^{M_2} \equiv u_2, u_3^{M_3} \equiv u_3$  and the tangential displacement  $u_1^{M_2} \equiv v$ . The overall deformation gradient is related to master node displacements through

$$\mathbf{F} = \begin{bmatrix} \frac{A}{A_0} & \frac{v}{B_0} & 0\\ 0 & \frac{B}{B_0} & 0\\ 0 & 0 & \frac{C}{A} \end{bmatrix}$$
 (17)

where the current average dimensions of the deformed unit cell are calculated as  $A = A_0 + u_1$ ,  $B = B_0 + u_2$ ,  $C = A_0 + u_3$ . Eq. (17) follows from

the definition of F as the volume average of its microscopic counterpart, the divergence theorem and the boundary conditions, Eq. (16).

The rate of deformation is then obtained as

$$\mathbf{D} = \operatorname{sym}(\dot{\mathbf{F}}\mathbf{F}^{-1}) = \begin{bmatrix} \frac{\dot{u}_1}{A} & \frac{1}{2} \left( \frac{\dot{v}}{B} - \frac{v\dot{u}_1}{AB} \right) & 0\\ \frac{1}{2} \left( \frac{\dot{v}}{B} - \frac{v\dot{u}_1}{AB} \right) & \frac{\dot{u}_2}{B} & 0\\ 0 & 0 & \frac{\dot{u}_3}{C} \end{bmatrix}$$
(18)

Nominally, the logarithmic rate of E is identified with D.

Proportional stressing (constant  $\rho$  and  $\kappa$  in Eq. (13) or, equivalently, constant T and L in Eq. (14)) is accomplished by introducing generalized nodal forces, which are work-conjugate with the master node displacements. Thus, if  $P_{ij}$  denotes the generalized force corresponding to degree of freedom i of master node j, the external power is:

$$\dot{W}_{\text{ext}} = P_{11}\dot{u}_1 + P_{22}\dot{u}_2 + P_{33}\dot{u}_3 + P_{12}\dot{v} \tag{19}$$

On the other hand, the Hill–Mandel lemma is adopted to write the internal power of the cell as:

$$\dot{W}_{\text{int}} = \Omega(\Sigma_{11}D_{11} + \Sigma_{22}D_{22} + \Sigma_{11}D_{33} + 2\Sigma_{12}D_{12}) \tag{20}$$

Substituting expressions for the rate of deformation, Eq. (18), results in

$$\dot{W}_{\text{int}} = \Omega \left[ \left( \frac{\Sigma_{11}}{A} - \frac{\Sigma_{12} v}{AB} \right) \dot{u}_1 + \left( \frac{\Sigma_{22}}{B} \right) \dot{u}_2 + \left( \frac{\Sigma_{11}}{C} \right) \dot{u}_3 + \left( \frac{\Sigma_{12}}{B} \right) \dot{v} \right]$$
(21)

Then, combining Eqs. (19) and (21) and using the principle of virtual work gives:

$$\begin{split} \left[P_{11} - \Omega\left(\frac{\Sigma_{11}}{A} - \frac{\Sigma_{12}v}{AB}\right)\right] \dot{u}_1 + \left(P_{22} - \Omega\frac{\Sigma_{22}}{B}\right) \dot{u}_2 + \left(P_{33} - \Omega\frac{\Sigma_{11}}{C}\right) \dot{u}_3 + \\ \left(P_{12} - \Omega\frac{\Sigma_{12}}{B}\right) \dot{v} = 0 \end{split}$$

(22)

for arbitrary displacements  $u_1$ ,  $u_2$ ,  $u_3$  and v. The generalized forces are thus obtained as:

$$P_{11} = \Omega \left( \frac{\Sigma_{11}}{A} - \frac{\Sigma_{12} v}{AB} \right) \qquad P_{22} = \Omega \left( \frac{\Sigma_{22}}{B} \right)$$

$$P_{33} = \Omega \left( \frac{\Sigma_{11}}{C} \right) \qquad P_{12} = \Omega \left( \frac{\Sigma_{12}}{B} \right)$$
(23)

The dependence of  $P_{11}$  upon the shear stress  $\Sigma_{12}$  is a finite strain effect in that the shear deformation gradient contributes to the normal stress along  $x_1$ .

Now, imposing constant ratios of generalized forces leads to constant stress ratios but imposition of the forces directly to the master nodes  $M_i$  is not possible since their displacements are constrained by Eq. (16). Hence, a penalty-like method is used whereby four springs are introduced to couple the four displacements of master nodes  $M_1, M_2, M_3$  with four displacements of dummy nodes  $N_1, N_2, N_3, N_4$ . With reference to Fig. 1a, the normal displacements are denoted:  $u_1^{N_1} \equiv U_1, u_2^{N_2} \equiv U_2, u_3^{N_3} \equiv U_3$  and the tangential displacement  $u_1^{N_4} \equiv V$ . The  $P_{ij}$ 's, identified with the forces in the springs, are then written in terms of dummy node displacements relative to master node displacements, namely:

$$P_{ii} = k(U_i - u_i)$$
 (no sum on i),  $P_{12} = k(V - v)$  (24)

where k is the spring stiffness chosen to be large enough to get a good force control.

Dividing the forces in Eq. (23) by any of them delivers three constraints on the master node displacements in terms of the stress ratios  $\rho$  and  $\kappa$  of Eq. (13). Then identification with the spring forces in Eq. (24) leads to constraints on both master and dummy node displacements. For instance, if the forces are normalized by a normal force, say  $P_{22}$ , the following constraints are obtained:

$$U_{1} - u_{1} = \left(\frac{\rho B}{A} - \frac{\kappa v}{A}\right) (U_{2} - u_{2})$$

$$U_{3} - u_{3} = \frac{\rho B}{C} (U_{2} - u_{2})$$

$$V - v = \kappa (U_{2} - u_{2})$$
(25)

By way of contrast, if the forces are normalized with respect to the shear force  $P_{12}$ , the constraints then read:

$$U_1 - u_1 = \left(\frac{\rho B}{\kappa A} - \frac{v}{A}\right)(V - v)$$

$$U_3 - u_3 = \frac{\rho B}{\kappa C}(V - v)$$

$$U_2 - u_2 = \frac{1}{\kappa}(V - v)$$
(26)

Recall that the current cell dimensions, A, B, C involve the normal master displacements (the  $u_i$ 's). Each of the above nonlinear systems of equations involves eight unknown displacements (the  $u_i$ 's and  $U_i$ 's in addition to tangential displacements v and V). One dummy displacement is used as a pilot. Eq. (25) or Eq. (26) each supplies three relations, which when added to the four boundary condition constraints, Eq. (16), provides sufficient relations for transmitting the desired loading scheme to the entire cell, given a pair  $(\rho, \kappa)$ . The procedure is iterative. Convergence is sensitive to both the spring constant k as well as the normalization scheme. It is found that for a low value of the shear stress ratio (nominally for  $\kappa < 0.75$ ) Eq. (25) should be used with  $U_2$  as the pilot displacement. On the other hand, Eq. (26) is used for  $\kappa \ge 0.75$  with V as the pilot displacement.

Also note that the spring stiffness k does not enter Eqs. (25) and (26) as it drops out during normalization. However, k does affect convergence through the pilot dummy displacement. It is generally found that a value about one tenth of the material's elastic modulus is adequate.

The constraints in Eq. (16) are implemented using the \*Equation option in ABAQUS. The task is simplified by using the set of

python scripts *Homtools* developed by Lejeunes and Bourgeois (2011). A custom-coded multi-point constraint ABAQUS subroutine was developed to account for either Eq. (25) or Eq. (26) depending on the value of  $\kappa$ . Finally, the inner surfaces of the void are paired to consider self-contact with normal behavior in case of void closure. Since this does not occur in the particular cases treated here, related details will be described elsewhere. In all calculations, linear C3D8 elements were used. In Fig. 1b, the number of elements is about 15,000, but the number increases to ~25,000 for a cell with a higher aspect ratio and to ~30,000 when mesh sensitivity is analyzed.

Each calculation was post-processed so that the void dimensions and volume were output at every time step. The void volume fraction (or porosity f) was calculated from the total volume of sound material and the current dimensions of the cell as in Koplik and Needleman (1988).

## 2.3. Post-processing

Unit cell analyses have extensively been used to infer measures of strain to failure and to analyze the competition between strain localization and void coalescence. However, the terms "failure", "onset of coalescence" and "localization" require precise definitions. Here, failure is defined as the ultimate loss of stress carrying capacity, marked with  $(\times)$  in Fig. 2. Failure in that sense unequivocally corresponds to (complete) void coalescence, regardless of details in the final linkup process.

An important concept is that of unhomogeneous yielding. It is intimately connected to the progression of elastic unloading in the cell, Fig. 2. This terminology was first introduced by Torki and Benzerga (2018) and recently revisited by Benzerga (2023). The "onset of void coalescence" is, on the other hand, ambiguous and shall not be used, unless reference is made to the literature's terminology. Unhomogeneous yielding may be mistaken for a bifurcation type strain localization (Rice, 1976). In this section, special care is given to precise definitions of various concepts and their relations will be analyzed for key stress states in Section 3.

## 2.3.1. Elastic unloading

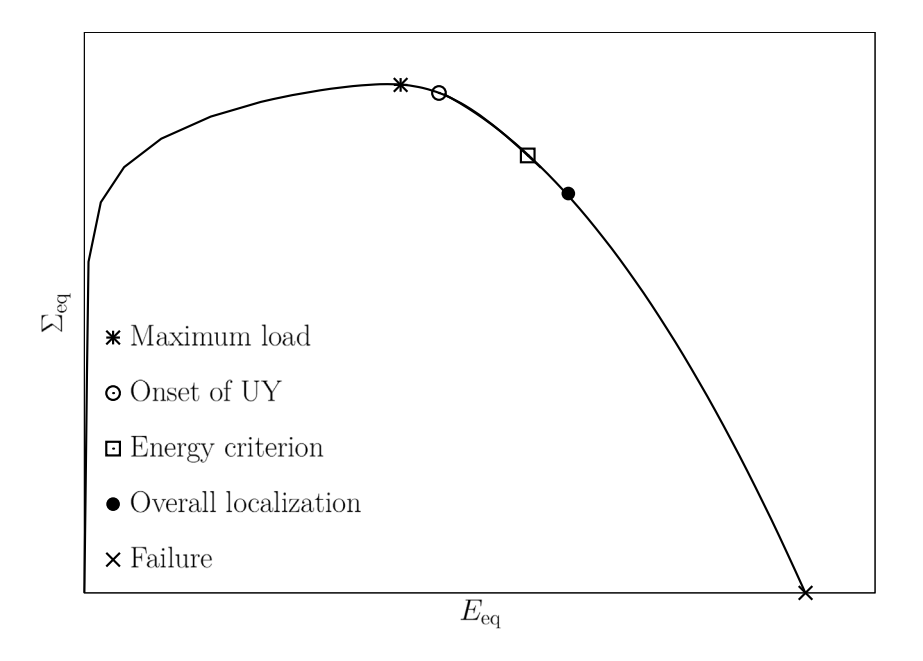
Elastic unloading occurs during void coalescence as well as outside of shear bands. Yet, it has only been analyzed in unit cell calculations through some overall signature, e.g. the transition to a uniaxial straining mode (Koplik and Needleman, 1988). Here, the aim is to follow the progression of elastic unloading in the unit cell by spatially mapping corresponding regions. With reference to the yield condition, Eq. (1), elastic unloading occurs when:

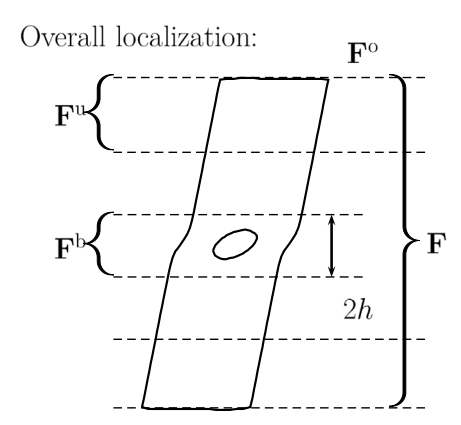
$$\phi(\sigma) = 0$$
 and  $\overset{\nabla}{\sigma} : \frac{\partial \phi}{\partial \sigma} < 0$  (27)

where  $\overset{\nabla}{\sigma}$  stands for the Jaumann rate of the Cauchy stress. A local material point is said to be elastically unloaded when the inner product of the stress increment and the outward normal to the yield surface is negative. The outward normal defines the direction of plastic flow, which is driven by the stress deviator for the  $J_2$  criterion used here, Eq. (2). In the numerical method, therefore, the inner product between the stress increment,  $\Delta \sigma$ , and the stress deviator  $\sigma'$  is used instead of Eq. (27):

$$\phi(\sigma) = 0$$
 and  $\Delta \sigma : \sigma' < 0$  (28)

In ABAQUS, the user-defined subroutine UVARM is used to extract current values of  $\sigma$  and the USDFLD subroutine is used to extract previous values of  $\sigma$ . Integration points where the condition (28) is satisfied are stored for visualization purposes, as sketched in Fig. 2.





Actual criterion:

$$\det\left(\mathbf{n}\cdot\mathbb{C}^t\cdot\mathbf{n}\right)=0$$

Surrogate criterion:

$$\frac{\|\dot{\mathbf{F}}\|}{\|\dot{\mathbf{F}}^{\mathrm{o}}\|} \to \infty$$



Unhomogeneous Yielding (UY)







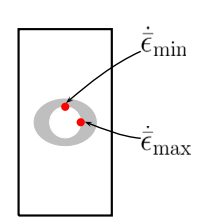


Fig. 2. Sketch of overall stress-strain response showing key instants, as marked. Regions painted black at bottom are elastically unloaded.

# 2.3.2. Unhomogeneous yielding

Unhomogenous yielding (UY) is nominally any stage in the deformation history where the elastically unloaded zones connect the lateral sides of the cell, Fig. 2. The presence of such zones precludes any lateral strain rate. Thus, for axisymmetric stress states, unhomogeneous yielding corresponds to the uniaxial straining mode of the cell. For these states, the onset of UY is therefore what has been referred to as "onset of void coalescence" in the literature (Benzerga and Leblond, 2010). By way of contrast, homogeneous yielding of the cell corresponds to that part of the response where the boundary strain-rate is nominally uniform; see Benzerga (2023) for discussion.

It is important to note that the so-defined regime of deformation corresponds to strong unhomogeneity. One can envision in theory, and realize in practice, macroscopically unhomogeneous deformation without elastic unloading. This is typical of the early stages of shear loading with hardening. Usually, such a regime manifests in transition. The reader is referred to Benzerga (2023) for details.

In the cell analyses, the onset of UY is detected by monitoring the elastically unloaded zones. On all subsequent curves, it will be marked with (o), Fig. 2.

### 2.3.3. Strain localization

A necessary condition for strain localization is Rice (1976)

$$\det \left( \mathbf{n} \cdot \mathbb{C}^{t} \cdot \mathbf{n} \right) = 0 \tag{29}$$

where n is the normal to the plane of localization, and  $\mathbb{C}^t$  is the tangent modulus entering the rate constitutive relation in terms of the first Piola–Kirchhoff stress, P, and deformation gradient F

$$\dot{\mathbf{P}} = \mathbb{C}^{t} : \dot{\mathbf{F}} \qquad \mathbf{P} = (\det \mathbf{F}) \ \boldsymbol{\Sigma}^{T} \mathbf{F}^{-T}$$
(30)

where  $\Sigma$  is given by Eq. (5) and rates are for rotated quantities.

As further discussed by Perrin and Leblond (1993), Rudnicki and Rice (1975) showed that, for isotropic behavior, the normal to the localization plane is always perpendicular to the direction of the intermediate principal stress. For the states of stress considered here (one shear stress and three normal stresses) the intermediate principal stress is along the direction  $e_3$ . Hence, n is always in the  $e_1-e_2$  plane. For convenience, in unit cell simulations, the normal to the localization plane is set along the direction  $\mathbf{n}=\mathbf{e}_2,$  and the major principal stress direction is changed so that a minimum strain to localization is obtained. Several unit cell studies (Barsoum and Faleskog, 2011; Tekoğlu et al., 2015; Vishwakarma and Keralavarma, 2019) explored such a critical plane for localization for several loading conditions. The normal to the critical plane of localization was found to be about  $45^{\circ}$ to the direction of the major principal stress for plane strain (L = 0). On the other hand, for axisymmetric loading (L = -1) all planes are equally critical, but a steep drop in effective stress was only observed at 0° to the major principal stress.

Of the three methods reviewed in the introduction for evaluating  $\mathbb{C}^t$ , we have implemented the perturbation technique (Temizer and Wriggers, 2008; Tchalla et al., 2013). The method is computationally expensive but is straightforward. Each component of  $\mathbb{C}^t$  is numerically obtained by perturbing the components of the macroscopic deformation gradient  $\mathbf{F}$ , one by one, from some current state:

$$\mathbf{F}' = \mathbf{F} + \delta F \mathbf{e}_k \otimes \mathbf{e}_l \tag{31}$$

 $\mathbf{e}_k$  and  $\mathbf{e}_l$  being the kth and lth unit vectors. The magnitude of the perturbation,  $\delta F$ , is the same for all components. It is chosen so that the elasto-plastic branch of  $\mathbb{C}^t$  is probed; see Appendix A. The response to the perturbation is then characterized by the average Piola stress components,  $P_{ij}$ , and the tangent moduli are determined using:

$$\forall i, j, k, l = 1, 2, 3, \qquad C_{ijkl}^{\rm t} = \frac{\delta P_{ij}}{\delta F_{kl}} = \frac{P_{ij}(\mathbf{F}') - P_{ij}(\mathbf{F})}{\delta F} \tag{32}$$

For illustration purposes, Eq. (32) may be structured in matrix form as follows:

Thus, perturbing the *i*th component of the deformation gradient allows to evaluate nine tangent moduli. Since, with the present setup, the normal to the localization band is  $\mathbf{n} = \mathbf{e}_2$ , only the second component of  $\mathbf{n}$  is non-zero. Hence, Eq. (29) reduces to:

$$\det\left(C_{2ik2}^{\mathsf{t}}\right) = 0\tag{34}$$

Thus, one need only perturb  $F_{12}$ ,  $F_{22}$ ,  $F_{32}$  to obtain the acoustic tensor.

In practice, the current deformation gradient F in Eq. (31) is extracted from the ABAQUS evolution problem with periodicity and proportional loading, Eq. (17). The problem is solved using the 'restart' option. After completion of the simulation, jobs are restarted three times at every increment in the deformation history. Each restart involves one perturbation calculation corresponding to the above three components of F. The perturbation simulation retains periodicity but proportional loading is relaxed. Therefore, a perturbation simulation is driven by the master nodes  $M_i$ . Consistent with Eq. (31), the perturbed displacements are:

$$\left(u_i^{M_j}\right)' = u_i^{M_j} + \delta F L_{0j} \tag{35}$$

where the initial lengths of the unit cell are written as  $L_{01} = L_{03} = A_0$ ,  $L_{02} = B_0$  for convenience. For each increment of the reference evolution problem and its corresponding perturbed states, the volume averaged Cauchy stress  $\Sigma$  and the master node displacements  $u_1, u_2, u_3, v$  are extracted using the user subroutine URDFIL. The current and perturbed deformation gradients  $\mathbf{F}$  and  $\mathbf{F}'$  are obtained from Eq. (17) and Eq. (31), respectively. The nominal stresses  $\mathbf{P}(\mathbf{F})$  and  $\mathbf{P}(\mathbf{F}')$  are calculated using Eq. (30)<sub>2</sub> and the tangent moduli using Eq. (32). With this data, the localization condition, Eq. (34), is evaluated at every step in the reference evolution problem. The instant when the determinant of the acoustic tensor is evaluated to first become negative is marked on the overall stress–strain curve using the symbol ( $\bullet$ ), Fig. 2.

## 2.3.4. Surrogate localization criterion

To date, most cell model studies that investigated strain localization did not directly probe Eq. (29). Instead, consistent with the spirit of localization theory (Rice, 1976), homogeneous strain conditions were assumed at some distance from the void, with corresponding deformation gradient  ${\bf F}^0$ . The farthest that  ${\bf F}^0$  may be estimated is at the top and bottom boundaries of the cell, Fig. 2. That is the choice made for instance by Barsoum and Faleskog (2007b) and Tekoğlu et al. (2015). On the other hand, Dunand and Mohr (2014) identified  ${\bf F}^0$  with the average deformation gradient in the top (or bottom) quarter of the cell, also see Dæhli et al. (2022). Such identification is again predicated on the basis of deformation being approximately homogeneous in the so defined upper (and lower) blocks. Since these are two different choices, the latter is denoted  ${\bf F}^u$  in Fig. 2.

Then, the localization condition is expressed in terms of some scalar measure of strain in the entire cell relative to it in the putatively

homogeneously deformed region1:

$$\frac{\|\mathbf{f}\|}{\|\dot{\mathbf{f}}^0\|} \to \infty \tag{36}$$

where  $\|\cdot\|$  stands for any appropriate norm, e.g. the Euclidean norm of corresponding 9-vectors. It is reasonably believed in the above works that the surrogate criterion, Eq. (36), corresponds to strain localization in the sense of Eq. (29).

In practice, the surrogate criterion is said to be met when the ratio in Eq. (36) reaches a critical value. Values in the range of 2-10 were typically used in the literature. It is easy to show, without calculation, that the results cannot be sensitive to the exact value of the critical ratio (beyond a value of 2 or so). In fact, the main issue with Eq. (36) is that it is surrogate to both strain localization and unhomogeneous yielding (see Section 2.3.2). The issue will be revisited in Section 4.

## 2.3.5. Energy criterion

With reference to the additive decomposition of the total rate of deformation d (see Section 2.1), the rates of elastic and plastic work for the cell are respectively given by:

$$\dot{W}^{e} \equiv \int_{\Omega} \boldsymbol{\sigma} : \mathbf{d}^{e} d\Omega, \qquad \dot{W}^{p} \equiv \int_{\Omega} \boldsymbol{\sigma} : \mathbf{d}^{p} d\Omega,$$
 (37)

Wong and Guo (2015) introduced two energy measures, one of which is definitely relevant to the so-called onset of void coalescence.2 Under axisymmetric loadings, the above authors noted that the onset of void coalescence, in the sense of a shift to a uniaxial straining mode of the cell, occurred when the ratio of elastic work rate to plastic work rate reached a negative minimum:

$$\dot{W}^{\rm e}/\dot{W}^{\rm p} < 0$$
 and minimum (38)

Based on this interesting observation, Wong and Guo (2015) adopted Eq. (38) as a criterion for detecting the "onset of void coalescence" under general loadings.

In practice, the total, elastic and plastic energies are determined using the \*ENERGY FILE option in ABAQUS. Then, user-defined subroutines such as URDFIL, UVARM, and USDFLD are combined to obtain the required work rates  $\dot{W}^{\rm e}$  and  $\dot{W}^{\rm p}$  entering Eq. (38). The instant when the criterion is met is marked using the symbol (□) on all subsequent curves, Fig. 2.

# 2.3.6. Maximum load criterion

The maximum equivalent stress is straightforward to extract from unit cell simulations. It is of interest because past the maximum the periodic pattern of voids is prone to shear band formation. As noted by Tvergaard (2012), the type of unit cell calculations employed here do not account for a shear band with a wavelength larger than the void spacing (i.e. the cell size). It is worth emphasizing that the present analyses do eventually account for shear band formation with a wavelength close to the void spacing. That is precisely what the localization condition, Eq. (29), is meant to probe.

The strain at which the maximum load is attained is marked in Fig. 2 and in subsequent results using the symbol (\*).

#### 2.3.7. Strain concentration around the void

Tekoğlu et al. (2015) considered a strain-based criterion to indicate the onset of coalescence, see Fig. 2 (sketch at bottom right). The onset of coalescence is defined as that point in history when the ratio of the maximum to the minimum effective plastic strain rate at the void surface reaches a critical value, Z:

$$\frac{\dot{\bar{\epsilon}}_{\max}}{\dot{\bar{\epsilon}}_{\min}} = Z \tag{39}$$

In their analyses, a critical value of Z = 15 was used.

# 2.3.8. Loss of full rankedness of $\dot{\mathbf{F}}$

Recently, Cadet et al. (2021) observed that void coalescence must be accompanied with a loss of full rankedness of the rate of the deformation gradient. When this occurs, **F** becomes singular (rank one for extension and rank two for shear). With this rationale as basis, they proposed the following criterion to detect "coalescence" in their terminology:

$$\delta \equiv \frac{\det \dot{\mathbf{F}}}{\det \dot{\mathbf{F}}^{\text{ref}}} = 0, \qquad \det \dot{\mathbf{F}}^{\text{ref}} = \dot{e}^3 / (1 + \dot{e}t)^3$$
 (40)

The determinant of  $\dot{\mathbf{F}}$  for the actual cell problem is normalized by some reference value in order to avoid numerical errors associated with small values of the determinant itself. The reference value is that taken under homogeneous deformation, which (Cadet et al., 2021) estimate for an isotropic rigid-plastic material as given by Eq.  $(40)_2$ . Here, t is time and  $\dot{\epsilon}$  represents a strain rate in the principal stress axes. For diagonal loadings (as in our tension case)  $\dot{\epsilon} = \dot{u}_2/B$ ; see Eq. (18). For general loadings (as in our shear case) there is no explicit expression in Cadet et al. (2021, 2022). We have used the maximum extension in the principal basis of D. The two definitions would meet for an isotropic material, but not necessarily in the cell shear simulations. This is unimportant for probing the criterion as it only affects how normalization is carried out.

## 3. Results

The focus being on comparing shear against tension states, we only present results for L = 0 (shearing states) and L = -1 (axisymmetric states) keeping the stress triaxiality ratio the same. In all subsequent calculations, T = 1. To a given (L, T) pair correspond many (possibly infinite) combinations of the  $(\rho, \kappa)$  pair of stress ratios. Anisotropy is unavoidable in unit cell calculations so that different  $(\rho, \kappa)$  combinations eventually deliver different results at fixed T and L. Here, the  $(\rho, \kappa)$  pair is chosen so as to obtain the worst condition (most favorable orientation n as per strain localization, Eq. (29)). In previous studies (Barsoum and Faleskog, 2011; Tekoğlu et al., 2015; Vishwakarma and Keralavarma, 2019) the critical normal was found to be near 45° to the major principal stress direction for L=0. On the other hand, for L=-1, all planes were found to be equally critical, but a steep drop in stress was observed at 0°.

Furthermore, for practical reasons, just like in previous analyses, the normal to the plane of localization is always set along the major loading direction  $\mathbf{n} = \mathbf{e}_2$  and the pair  $(\rho, \kappa)$  is adjusted so as to make that orientation critical. Here, therefore, the axisymmetric case (L = -1,T=1) is obtained using  $\rho=0.4$  and  $\kappa=0$  for which the major principal stress direction corresponds to the main loading direction  $e_2$ . The shearing case (L = 0, T = 1) is obtained using  $\rho = 1.0$ and  $\kappa = 0.5774$ , which correspond to the maximum shear condition, such that the major principal stress direction is at 45° to e2. In the localization analyses, the magnitude of the perturbation  $\delta F$  entering Eq. (31) was taken equal to  $10^{-6}$ . A rationale is given in Appendix A.

Other parameters that remain fixed are: E = 210 GPa, v = 0.3,  $\sigma_0 =$ 420 MPa,  $\epsilon_0 = 0.002$ . In order to make contact with other similar studies, we have used a cell aspect ratio  $\lambda_0 \equiv B_0/A_0$  different from unity, but some calculations were carried out using  $\lambda_0 = 1$ . Two values of the

<sup>&</sup>lt;sup>1</sup> Needleman and Tvergaard (1992) introduced a criterion of this type for rate-dependent materials for which a bifurcation type localization, such as Eq. (29), is not possible and localization can only be studied in terms of the growth of perturbations.

<sup>&</sup>lt;sup>2</sup> The second measure,  $W^p/W^e$ , exhibits a maximum which Wong and Guo (2015) identify with "final void coalescence". Void coalescence, that is void linkup, is impossible to simulate in unit cell calculations without remeshing. The behavior they notice appears to be an artifact due to numerical stiffening as the elements in the ligament get squeezed and distorted.

strain hardening exponent were used: N=0 (ideally plastic matrix) and N=0.1. A range of values of the initial porosity was explored with a minimum of  $f_0=0.0005$  and a maximum of  $f_0=0.00353$ . For reference, previous unit cell studies that explored shearing states did not consider values of  $f_0$  lower than 0.001.

### 3.1. Axisymmetric versus shear loading

## 3.1.1. Axisymmetric states

Cell responses in terms of the overall equivalent stress,  $\Sigma_{\rm eq}$ , versus equivalent strain,  $E_{\rm eq}$  as per Eq. (7), and corresponding porosity evolution curves are shown in Fig. 3 for  $f_0=0.001$  and  $\lambda_0=1$ , for both the non-hardening and hardening matrices. Note that the capacity of the cell to deform past the load maximum is much greater in the non-hardening material. As is well known, this shows that geometry changes are more important than matrix hardening. There is an extensive literature on the case of axisymmetric loading going back to Koplik and Needleman (1988) including the effect of strain hardening in slowing down void growth, Fig. 3b.

Fig. 4 depicts the progress of elastic unloading, as per Eq. (27), inside the cell with a non-hardening matrix. The elastically unloaded regions are painted black in the figure whereas regions of plastic loading are painted gray. The various stages shown are marked on the corresponding N=0 curves in Fig. 3. Stages a-f correspond to an overall homogeneous deformation and the overall axial strain is compensated by uniform lateral contractions of the cell. Pockets of elastic unloading are observed as early as about stage c (well after the maximum of  $\Sigma_{eq}$  for N=0) above and below the void, but that elastic unloading has no overall signature. As deformation proceeds, elastic unloading suddenly fills the top and bottom layers of the cell. The bottom row of stages g-j in Fig. 3 typifies unhomogeneous yielding of the cell, as defined in Section 2.3.2. The elastically unloaded zones preclude any plastic contraction of the cell and deformation shifts to the well-known uniaxial straining mode. Uniaxial straining is the manifestation of unhomogeneous yielding in tension. To accommodate the overall uniaxial mode, porosity grows much faster after the onset of unhomogeneous yielding at about stage g. The growth is essentially lateral and is bound to lead to void coalescence. Void growth acceleration leads to a faster drop in the load bearing capacity of the cell. This illustrates the process of failure by internal necking of the intervoid ligament, which prevails in tension. The entire process is well reproduced by micromechanical models (Benzerga, 2002).

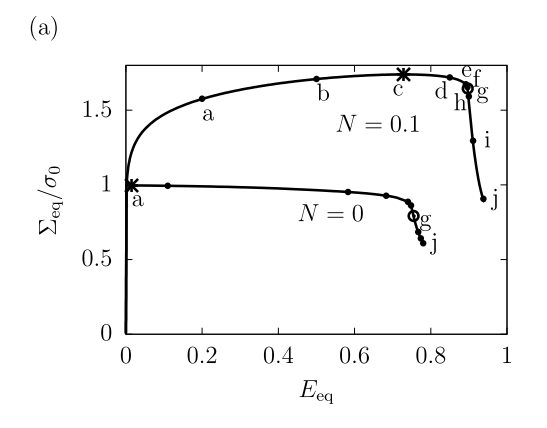
If the matrix material has some strain hardening capacity, then the overall response exhibits overall hardening up to stage c, Fig. 3a, and porosity growth is slower, Fig. 3b. The progression of elastic unloading in this case is shown in Fig. 5. The main difference between the N=0 case in Fig. 4 and the N=0.1 case in Fig. 5 is the extent of deformation, consistent with the effect of hardening on overall

ductility. However, the phenomenology of failure is the same as with no hardening, compare Fig. 5 with Fig. 4. In both cases, the cell deforms homogeneously through stage f, then when elastic unloading connects the lateral sides of the cell, unhomogeneous yielding prevails with the same features of uniaxial straining, fast porosity growth and abrupt load drop.

## 3.1.2. Shearing states

The overall responses under shear loading are plotted in Fig. 6a for a slender cell with  $\lambda_0 = 4$  and  $f_0 = 0.00353$  using the same equivalent stress and strain in Eq. (7). The corresponding porosity versus  $E_{\rm eq}$ curves are shown in Fig. 6b. Results are shown for the non-hardening material (N = 0) and the hardening material (N = 0.1). The capacity of the N=0.1 cell to deform past the load maximum is much greater in shear than in tension (compare with Fig. 3a). Another difference is in the rate of porosity growth. Interestingly, hardening induces a slowdown in porosity growth in the early stages. However, after a strain of  $E_{\rm eq} \approx 0.02$  the rate of growth becomes lower in the nonhardening matrix material, Fig. 6b. This is in clear contrast with the axisymmetric tension case in Fig. 3b. Note in passing that the rate of softening (past the maximum load) in Fig. 6a is higher for the hardening material. This is consistent with a faster void growth in the N=0.1cell, Fig. 6b. Also, the porosity increase in the non-hardening material is too modest to explain the softening seen in Fig. 6a. As is well known, the geometry change that affects shear softening is not volumetric growth, but rather void shape change and rotation. Both calculations in Fig. 6 were pursued until extreme element distortion no longer made calculations possible without remeshing.

Fig. 7 shows the progression of elastic unloading in the cell with a non-hardening matrix. As above, elastically unloaded elements are painted black. Other regions (essentially with plastic loading) are painted gray. The stages shown in the figure correspond to the various markings on the stress-strain and porosity strain curves in Fig. 6 for N=0. Unlike the nonhardening case in tension (Fig. 4) all stages correspond to unhomogeneous yielding, as defined in Section 2.3.2. In shear with no hardening, unhomogeneous yielding clearly prevails from the outset of plastic flow (stage a). Here too, the elastically unloaded zones preclude any plastic contraction of the cell but the latter has an extra degree of freedom that allows sliding of the top and bottom blocks relative to each other. This sliding mode of unhomogeneous vielding is void mediated, but the process can be (approximately) volume-preserving. The sliding mode is another manifestation of unhomogeneous yielding that operates in shear. Plastic deformation is confined to the band ligament whose thickness is comparable with the void size. Inside the band, void boundaries shear while porosity growth is limited. The void elongates and rotates such that the faces of the neighboring voids become closer together. Unlike in Tvergaard's early work (2008, 2009) difficulties associated with void closure induced



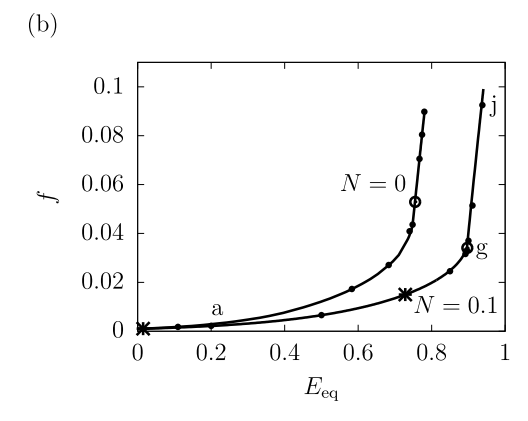


Fig. 3. (a) Overall equivalent stress,  $\Sigma_{\rm eq}$  as per Eq. (7), normalized by the initial yield stress  $\sigma_0$ , versus equivalent strain,  $E_{\rm eq}$ , and (b) Porosity, f, versus  $E_{\rm eq}$  for axisymmetric loading (T=1, L=-1),  $f_0=0.001$ ,  $\lambda_0=1$  and two values of the hardening exponent N. Snapshots corresponding to a-j markings are shown in Figs. 4 and 5.

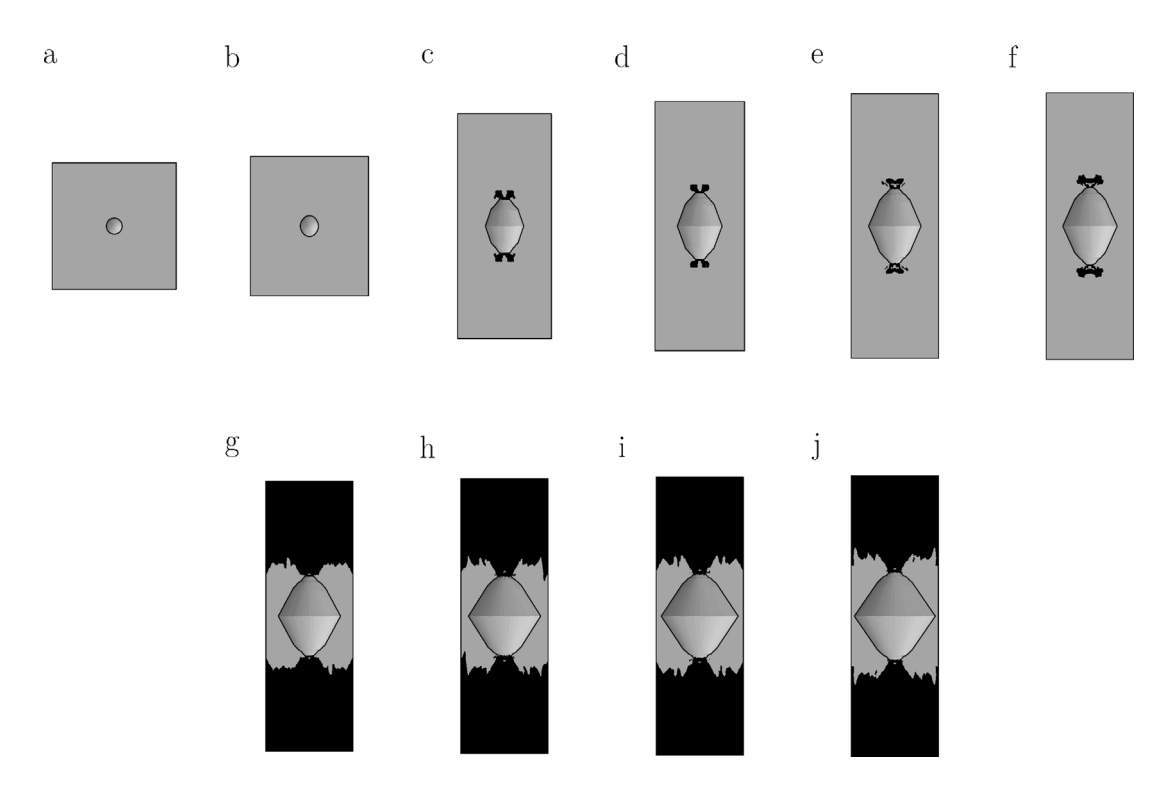


Fig. 4. Mid-section  $(x_3=0)$  of deformed cell at stages a–j marked on Fig. 3 for non-hardenable material (N=0). Regions painted black undergo elastic unloading. Case of axisymmetric tension (T=1,L=-1) with  $f_0=0.001$  and  $\lambda_0=1$ .

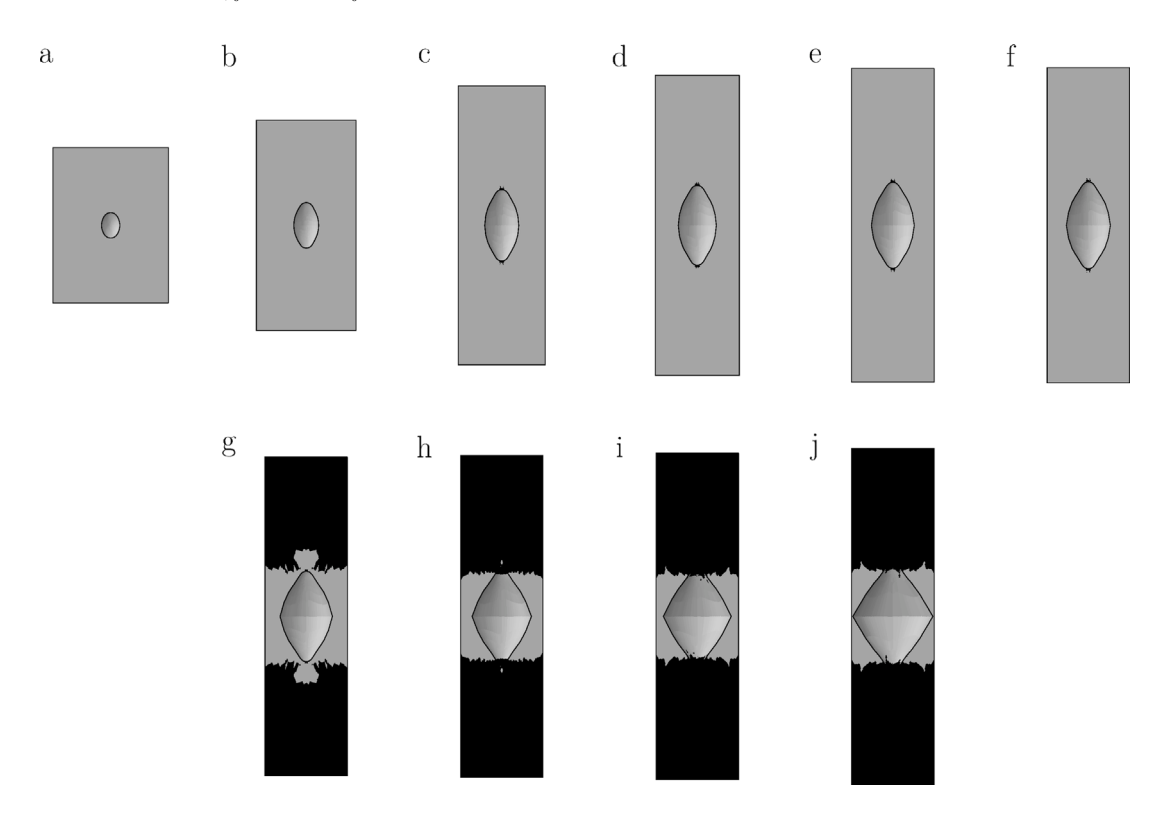


Fig. 5. Mid-section ( $x_3=0$ ) of deformed cell at stages a-j marked on Fig. 3 for hardenable material (N=0.1). Regions painted black undergo elastic unloading. Case of axisymmetric tension (T=1, L=-1) with  $f_0=0.001$  and  $\lambda_0=1$ .

contact are avoided thanks to the moderate value of T=1. Yet, even at such triaxiality, the essence of the deformation process is shear dominated. In such case, the porosity f is not the primary variable

that dictates softening. Instead, a parameter that quantifies ligament size plays a key role. A precise definition of that is beyond the scope here but if  $\chi_0 = r_0/A_0$  is the ratio of initial void size to lateral

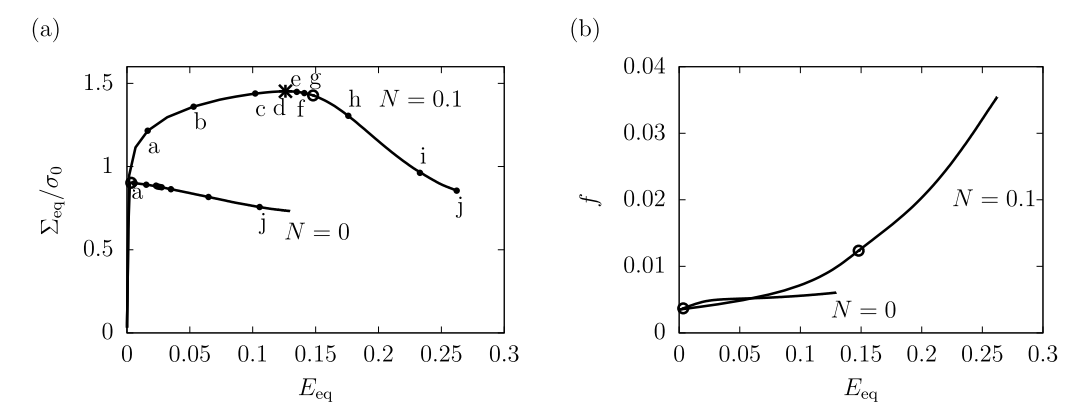


Fig. 6. (a) Overall equivalent stress,  $\Sigma_{\rm eq}$ , normalized by the initial yield stress  $\sigma_0$ , versus equivalent strain,  $E_{\rm eq}$ , and (b) Porosity, f, versus  $E_{\rm eq}$  for shear-dominated loading  $(T=1,L=0),\ f_0=0.00353,\ \lambda_0=4$  and two values of the hardening exponent N. Snapshots corresponding to a-j markings are shown in Figs. 7 and 8.

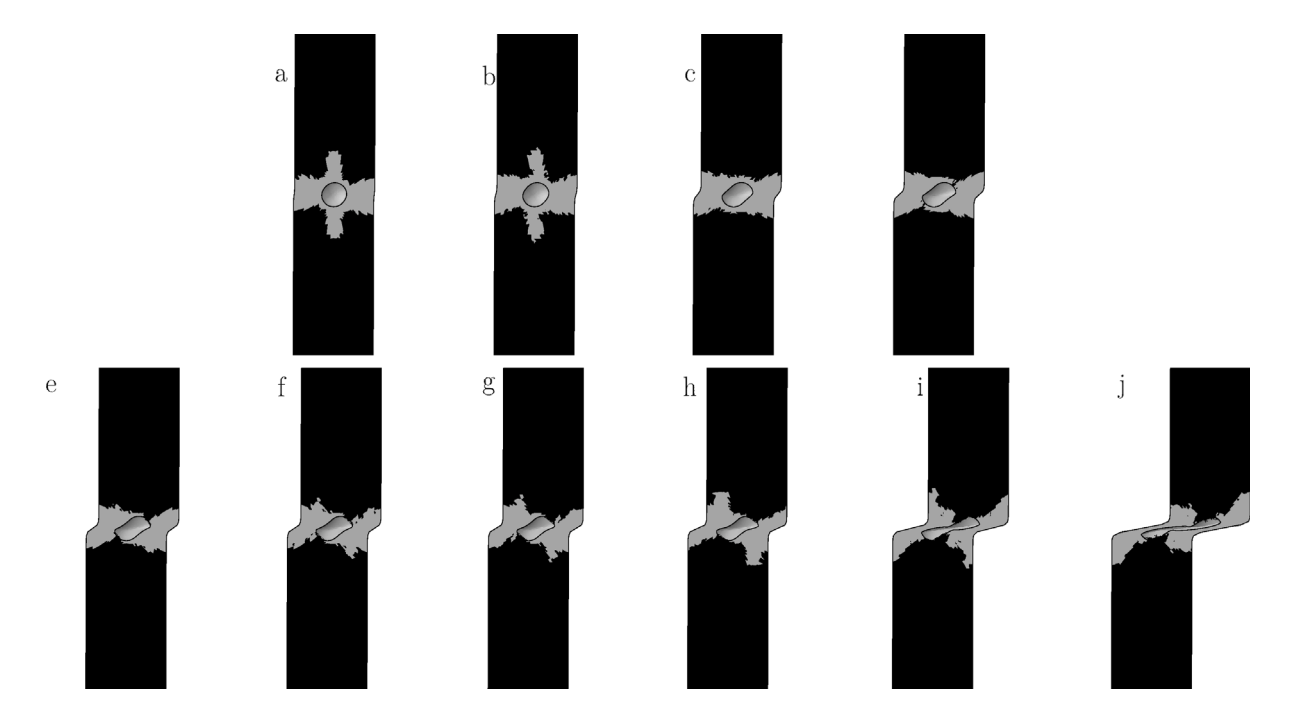


Fig. 7. Mid-section ( $x_3 = 0$ ) of deformed cell at stages a–j marked on Fig. 6 for the non-hardening material (N = 0). Regions painted black undergo elastic unloading. Case of shear-dominated loading (T = 1, L = 0) with  $f_0 = 0.00353$  and  $\lambda_0 = 4$ .

void spacing then  $1 - \chi_0$  represents the amount of material in the initial ligament. That value is initially 0.7 and reduces due to void shearing. That is the main source of softening. The process of softening in shear is qualitatively well reproduced using recent micromechanical models (Torki and Benzerga, 2018).

The situation is quite different in the hardenable material, Fig. 8. Here, unhomogeneous yielding does not set in until stage g. Recall that unhomogeneous yielding is active when the elastically unloaded zone connects the lateral sides of the cell (percolation). Similar to tension, the early stages are characterized by diffuse plastic flow (gray zones extend below and above the void in the top row of Fig. 8) but now with nominally unhomogeneous deformation. The upper and lower blocks deform at a lower rate than the ligament. Contrary to tension, however, there is a more gradual progression of elastic unloading in the cell. Elastic unloading begins as early as stage d (interestingly near the maximum load) and proceeds in an asymmetric mode (stages d through f). When for the first time the two regions of elastic unloading in the upper (or lower) block connect at stage g, unhomogeneous yielding sets in with now the strain rate parallel to the band vanishing. Upon further straining, the elastic unloading regions spread toward the void (h-j).

The ensuing softening process is still a challenge for micromechanical modeling.

## 3.1.3. Failure locus

In the previous section, the process of elastic unloading and the related notion of unhomogeneous yielding were analyzed in some detail for both axisymmetric and shearing states. In doing so, the employed geometries were similar to those used in previous studies, cubic cell ( $\lambda_0=1$ ) for axisymmetric loading and tetragonal cell ( $\lambda_0>1$ ) for shear loadings. To address the main question of the paper, however, comparison between axisymmetric and shearing states must be performed for the same initial geometries. This task is undertaken in this section for two initial geometries: ( $f_0=0.00353, \lambda_0=4$ ) and ( $f_0=0.0005, \lambda_0=1$ ). The first typifies "high porosity" behavior and the second "low porosity" behavior. In both cases, the strain hardening exponent is N=0.1.

Next, a measure of strain to failure is required for the comparison. As seen from Fig. 3, the onset of unhomogeneous yielding is an appropriate measure of failure under axisymmetric loading because of the subsequently abrupt load drop. However, the onset of unhomogeneous

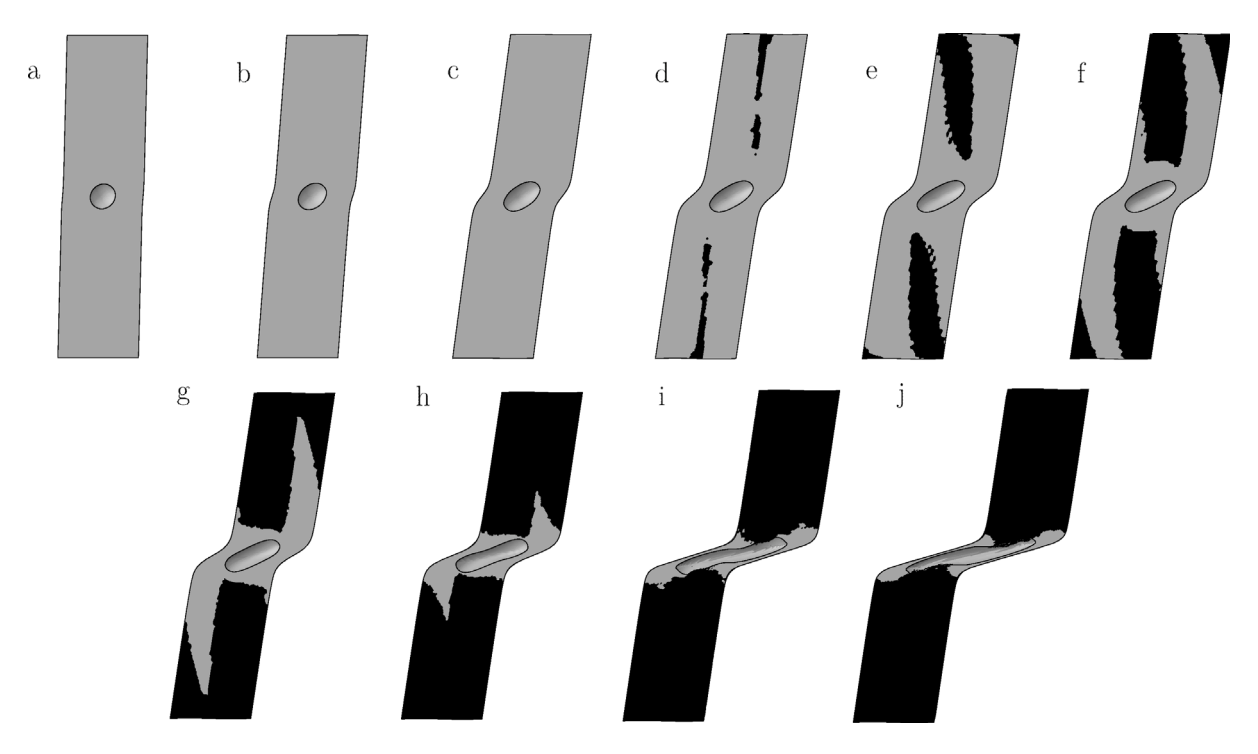


Fig. 8. Mid-section ( $x_3=0$ ) of deformed cell at stages a-j marked on Fig. 6 for the hardening material (N=0.1). Regions painted black undergo elastic unloading. Case of shear-dominated loading (T=1, L=0) with  $f_0=0.00353$  and  $\lambda_0=4$ .

yielding is not in any way a measure of failure under shear loadings, irrespective of the hardening capacity of the material, see Fig. 6.

An alternative critical measure of ductility that has extensively been (meant to be) used in the literature is the strain to localization,  $E_{\rm eq}^{\rm L}$ , which is determined from Eq. (29) by the perturbation method of Section 2.3.3. The values of  $E_{\rm eq}^{\rm L}$  are reported in Fig. 9a for both loading conditions (L=-1 and L=0) and both sets of initial geometries. Values of the strain to the onset of unhomogeneous yielding,  $E_{\rm eq}^{\rm LY}$ , are also reported for comparison. Fig. 9a reports a key finding. In the "high porosity" case ( $f_0=0.00353$ ), strain localization occurs at a lower strain in shear (L=0) than in tension (L=-1), consistent with available cell model results. However, in the "low porosity" case ( $f_0=0.0005$ ), the opposite trend is obtained with the strain to localization increasing from axisymmetric tension to shear. This finding is robust upon further mesh refinement.

The overall stress–strain responses and corresponding porosity evolution for the "high porosity" cell are shown in Fig. 10. The shear (L=0) case is the same as in Fig. 6. The onset of unhomogeneous yielding is indicated by (o) and corresponds to stage (g) in Fig. 8. Strain localization, which is marked using the symbol (•) in Fig. 10, occurs beyond the onset of unhomogeneous yielding. On the other hand, in tension (L=-1) unhomogeneous yielding and strain localization are essentially concurrent. In fact, we verify that the former occurs first and in the subsequent increment the determinant in Eq. (34) vanishes.

Prior to the onset of unhomogeneous yielding, porosity growth is faster in shear than in tension (Fig. 10b) for the stress triaxiality considered (T=1). A qualitative explanation for this is that void shearing (Fig. 8) reduces the ligament size faster in comparison with tension. It also exposes more void surface to the axial tensile stress. However, after the onset of unhomogeneous yielding the rate of porosity growth in tension far exceeds that in shear. This is an important distinction between the two stress states. Neither unhomogeneous yielding nor strain localization lead to an abrupt acceleration of void growth or to a load drop in shear, unlike tension.

For the "low porosity" case (Fig. 11), the shear and tension stress-strain curves are indistinguishable until  $E_{\rm eq}\approx 0.7$ . Unhomogeneous yielding still occurs earlier in shear ( $E_{\rm eq}^{\rm UY}=0.75$ ) than in tension

 $(E_{\rm eq}^{\rm UY}=0.87)$ . Strain localization, on the other hand, is concurrent with unhomogeneous yielding in tension but occurs later in shear  $(E_{\rm eq}^{\rm L}=0.95)$ . By way of consequence, we now have a situation where strain localization occurs earlier in tension than in shear. The difference may not appear to be large. Note, however, the strain levels reached in this case  $(E_{\rm eq}\sim 1.0)$  in comparison with those in the high porosity case of Fig. 10  $(E_{\rm eq}\sim 0.2)$ . The absolute difference between the strains to localization in shear and tension is about the same for the high and low porosity cases; it is just that the order reverses. This is reflected in the slope inversion in Fig. 9a. Such a trend is apparently shown for the first time.

In terms of porosity growth, Fig. 11b, the f versus  $E_{\rm eq}$  curves fall nearly on top of each other prior to  $E_{\rm eq}\approx 0.5$ . In fact, the rate of growth of porosity is somewhat lower in shear than in tension, unlike the high porosity case; see Fig. 10b. Eventually, the rate of growth becomes larger in shear. Qualitatively, these trends are explained as follows. The ligament size does not reduce as fast in shear for the low porosity case because shearing a small void may bring void closure earlier. Actual closure is here avoided given that T=1. As in the high porosity case, the onset of unhomogeneous yielding does not lead to void growth acceleration, unlike tension.

In all cases considered (including with a non-hardening matrix), the softening after the onset of unhomogeneous yielding in shear is weaker than in tension. The same observation holds post-localization. It is possible that in an actual material, the onset of strain localization would lead to more immediate failure. But that is only a 'belief'. Multi-void, large scale simulations may shed light on this. However, it should not be taken for granted that the post-localization behavior in shear would lead to as much softening as in tension. Therefore, it is only legitimate to also report strains to failure, understood as defined in Fig. 2, namely at void coalescence where all stress carrying capacity of the cell would vanish. That state cannot be reached in the present cell calculations. One would need either remeshing or arbitrary lagrangian-eulerian formulations (Becker, 2017). It is tempting, however, to extrapolate the present results assuming constant softening to failure. The point at which the extrapolated stress-strain curve reaches the zero stress axis is represented by  $\times$  in Fig. 2 and the corresponding strain is denoted  $E_{\rm eq}^{\rm f}$ 

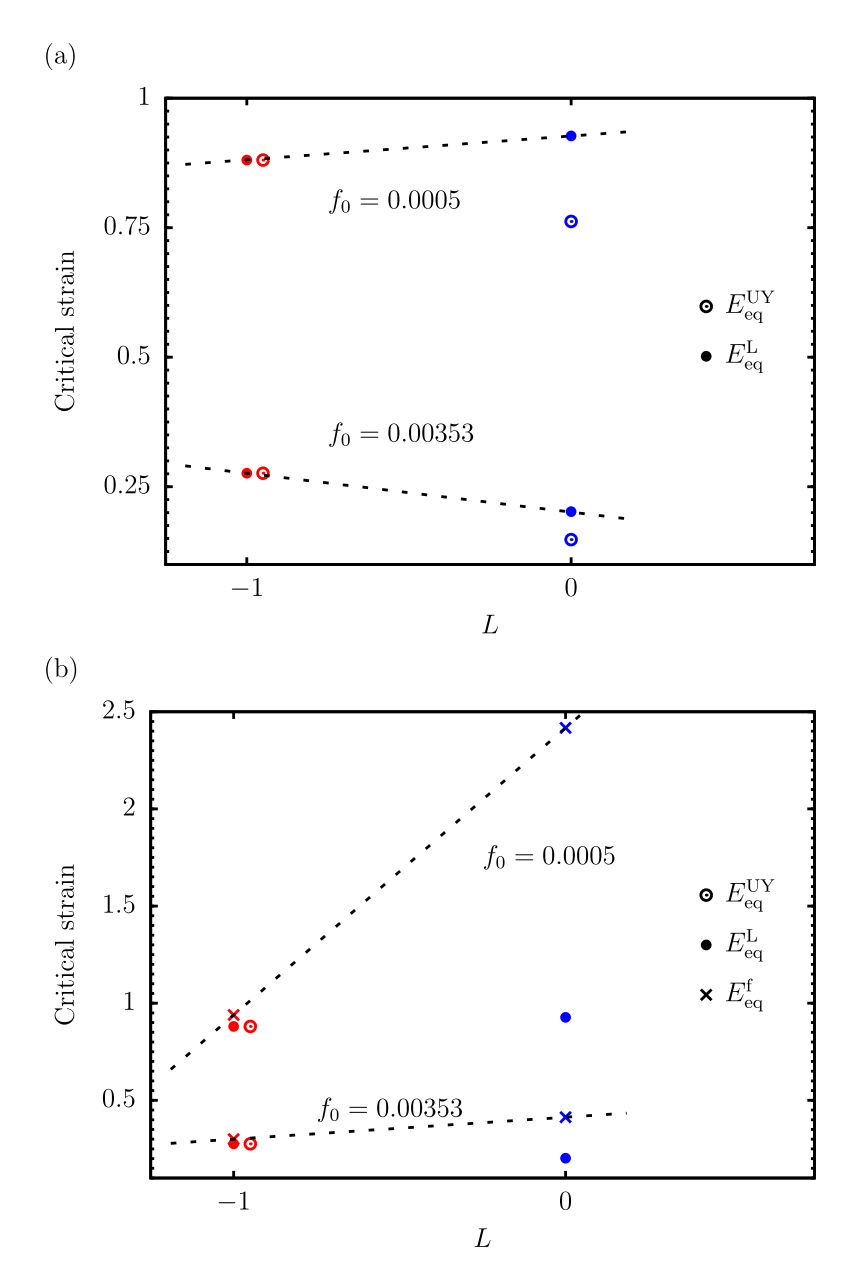


Fig. 9. Trend lines (dashed) for failure loci using two critical strain measures: (a) Strain to localization,  $E_{eq}^L$ , given by Eq. (29) and the perturbation method. (b) Strain to failure,  $E_{eq}^L$ , by extrapolation to complete loss of stress carrying capacity of the cell; see Fig. 2. The strain to the onset of unhomogeneous yielding,  $E_{eq}^{UY}$ , is included for reference.

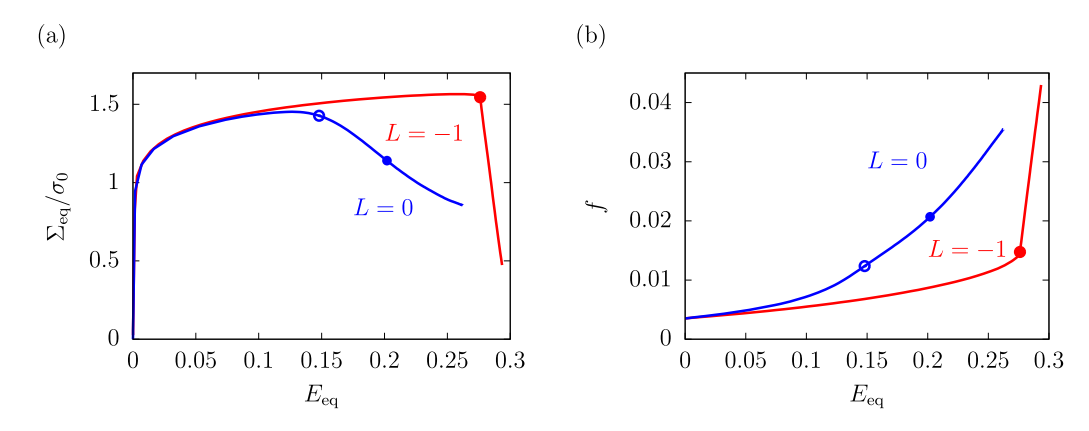
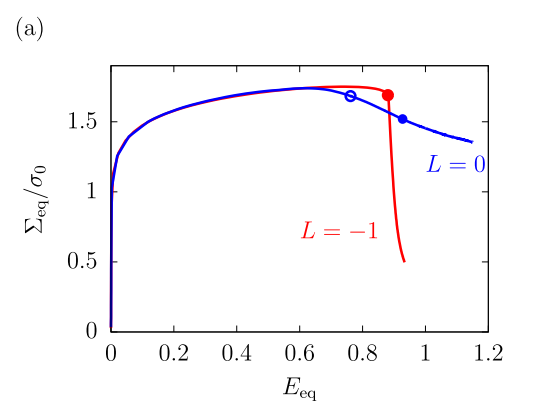


Fig. 10. (a) Overall normalized equivalent stress,  $\Sigma_{\rm eq}/\sigma_0$ , versus equivalent strain,  $E_{\rm eq}$ , and (b) Porosity, f, versus  $E_{\rm eq}$  for a "high porosity" case ( $f_0=0.00353$ ,  $\lambda_0=4$ ) comparing the onset of unhomogeneous yielding ( $\circ$ ) and strain localization ( $\bullet$ ) for axisymmetric loading (L=-1) and shear loading (L=0).



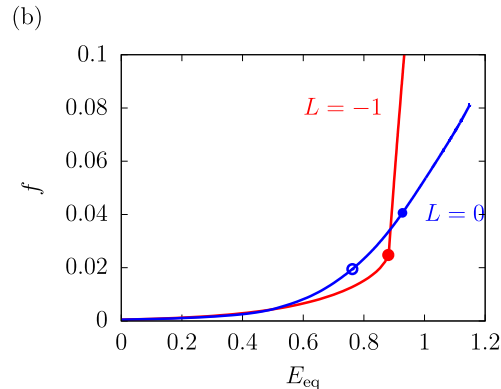


Fig. 11. (a) Overall normalized equivalent stress,  $\Sigma_{\rm eq}/\sigma_0$ , versus equivalent strain,  $E_{\rm eq}$ , and (b) Porosity, f, versus  $E_{\rm eq}$  for a "low porosity" case ( $f_0 = 0.0005$ ,  $\lambda_0 = 1$ ) comparing the onset of unhomogeneous yielding (o) and strain localization (•) for axisymmetric loading (L = -1) and shear loading (L = 0).

(see Section 3.2.3 for an illustration of the construction). The results are superposed on previous ones in Fig. 9b.

Interestingly, considering the strain to failure measure  $E_{\rm eq}^{\rm f}$ , shearing states are found to be more ductile than axisymmetric states at both porosity levels. This trend reflects the much emphasized difference between rates of softening in shear versus tension. The trend reversal is particularly important for the low porosity case, Fig. 9b.

## 3.2. Void coalescence versus strain localization

It is clear thus far that the onset of unhomogeneous yielding under axisymmetric loadings signifies what has been referred to in the literature as the "onset of void coalescence" in the sense of a shift to uniaxial straining accompanied with internal necking. Unhomogeneous yielding is, however, a more general concept encompassing axisymmetric as well as shearing states. The results in the previous section demonstrate that, in general, unhomogeneous yielding precedes strain localization. This finding contrasts with claims made elsewhere insofar as "void coalescence" and unhomogeneous yielding are used interchangeably. To bring clarity into this, the various measures of critical strains that were introduced in the literature (see Section 2.3) are compared in this section.

## 3.2.1. Unhomogeneous yielding coincides with strain localization

Under axisymmetric loading, as soon as unhomogeneous yielding sets in strain localization occurs; see Figs. 10 and 11. In such cases, it is verified that the energy criterion of Eq. (38) is concurrent with the onset of unhomogeneous yielding. This is illustrated in Fig. 12 for a case with  $f_0=0.001, \lambda_0=1$ . The stress–strain curve is shown in Fig. 12a, the evolution of overall logarithmic strains in Fig. 12b and the evolution of the rate of elastic work in Fig. 12c. When the cell's deformation mode shifts to uniaxial straining ( $\dot{E}_{11}=0$ ) the rate of elastic work does reach a negative minimum, as per Eq. (38). This finding is consistent with the work of Wong and Guo (2015). Fig. 12d shows that the incipient state is one of unhomogeneous yielding with elastic unloading connecting the lateral sides above and below the void. Under axisymmetric loading, therefore, unhomogeneous yielding (which is equivalent to uniaxial straining for that loading), strain localization and a negative minimum in the rate of elastic work all coincide.

Next, consider the surrogate localization criterion of Eq. (36). The ratio  $\|\dot{\mathbf{F}}\|/\|\dot{\mathbf{F}}^0\|$  is plotted against the cell's equivalent strain in Fig. 13a. As above, the symbol ( $\circ$ ) represents the onset of unhomogeneous yielding, which coincides with strain localization as per Eq. (29). As expected, the criterion in Eq. (36) may be viewed as surrogate to both unhomogeneous yielding and strain localization. As anticipated, whether a critical value of 2 or above is used would negligibly affect the critical strain.

The criterion introduced by Tekoğlu et al. (2015), which is based on the ratio of maximum to minimum plastic strain around the void, Eq. (39), is evaluated in Appendix B. It is shown there that arbitrary values are obtained for the "coalescence strain" depending on the chosen critical value of Z.

The loss of full rankedness parameter  $\delta$ , introduced by Cadet et al. (2021) and given by Eq. (40), is plotted in Fig. 13b. After a transient about the elastic–plastic transition, the parameter slightly increases then decreases, steadily at first then abruptly at  $E_{\rm eq} \sim 0.9$ . After this critical strain value, it vanishes, as expected during uniaxial extension. The open circle in Fig. 13b corresponds, as above, to the onset of unhomogeneous yielding. Thus, in tension the loss of full rankedness of F corresponds exactly to the onset of unhomogeneous yielding.

In conclusion, with the exception of the criterion of Tekoğlu et al. (2015), all of the above criteria deliver the same value of the critical strain in tension.

# 3.2.2. Unhomogeneous yielding precedes strain localization

Under shear-dominated loading, unhomogeneous yielding was found to precede strain localization; see Figs. 10 and 11. For such stress states, we first investigate what the energy criterion of Eq. (38) predicts. Results are reported in Fig. 14 for the two cases that were previously analyzed in Fig. 6.

For the hardening matrix (N=0.1), unhomogeneous yielding (see  $\circ$  in Fig. 14a) occurs shortly after the load maximum. The corresponding incipient state is shown in Fig. 14d. The overall strain components, as defined in Eqs. (8)–(11), are plotted against  $E_{\rm eq}$  in Fig. 14b. Unlike the axisymmetric loading case, the lateral strain components ( $E_{11}, E_{33}$ ) do not saturate because of the presence of the shear term in the Eulerian strain expressions, Eqs. (8) and (10). However, the lateral rate of deformation,  $D_{11}$  in Eq. (18), essentially vanishes (not shown in order not to clutter the plot).

The corresponding rate of change of the elastic energy in the cell is plotted in Fig. 14c. The profile is quite different from the tension case; see Fig. 12c. Eventually, a global negative minimum is attained, indicated by a ( $\square$ ), but the decrease of  $dW^e/dW^p$  is more gradual in shear than in tension. Also, the spread of values about the minimum is wider than in tension. Most importantly, the negative minimum is attained well after the onset of unhomogeneous yielding, but before strain localization.

Similar conclusions are reached for the non-hardening case with the minimum of  $dW^e/dW^p$  being attained in a subtle way, Fig. 14c. Thus, for shear loading conditions, regardless of the matrix hardening capacity:

The onset of unhomogeneous yielding corresponds to the vanishing of the components of D parallel to the band.

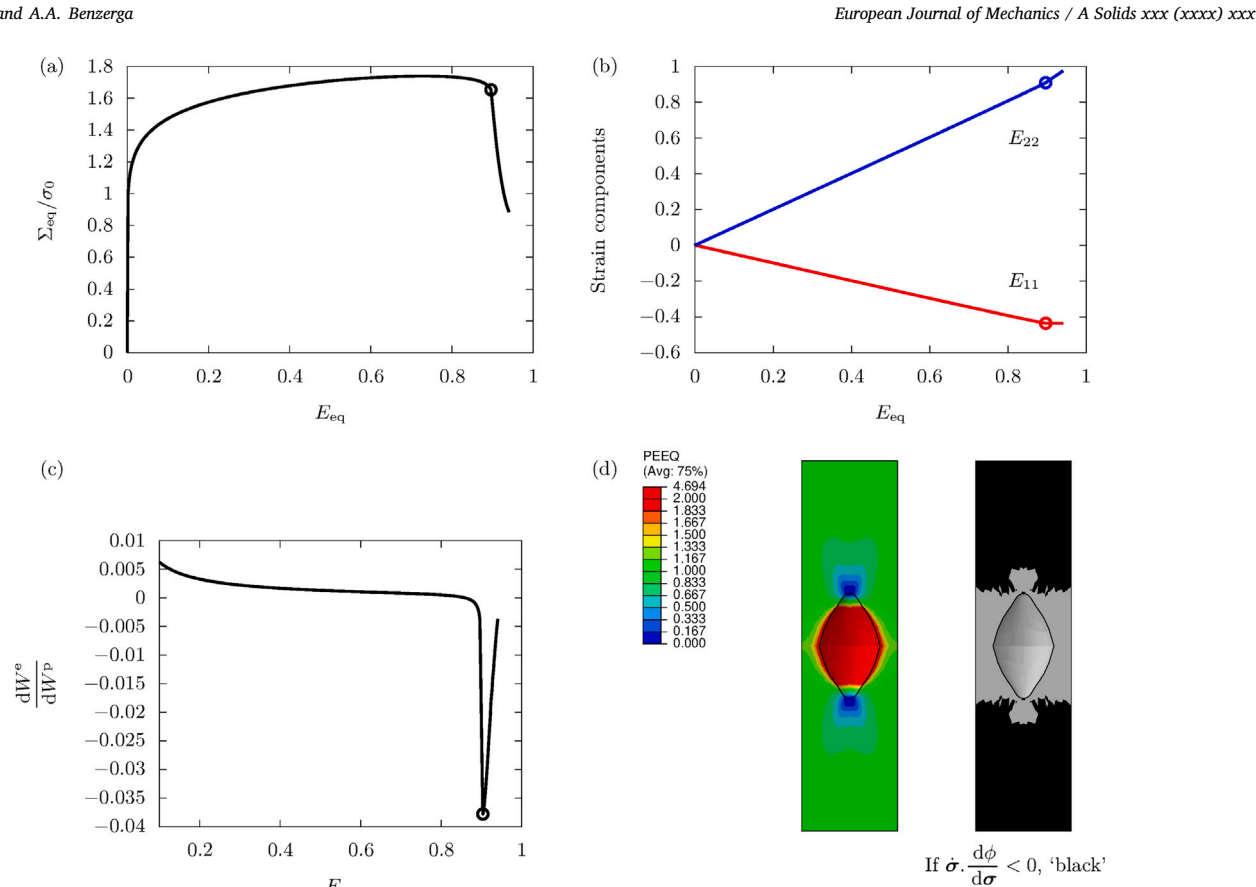


Fig. 12. (a) Overall stress-strain response and corresponding evolution of (b) the overall logarithmic strains, and (c) the rate of change of elastic energy of the unit cell for axisymmetric loading (T=1, L=-1),  $f_0=0.001$ ,  $\lambda_0=1$  and N=0.1. (d) Deformed configuration at the onset of unhomogeneous yielding, marked with (o) in (a)–(c), showing contours of effective plastic strain  $\bar{\epsilon}$  (left) and regions of elastic unloading (painted black; right).

 $E_{\rm eq}$ 

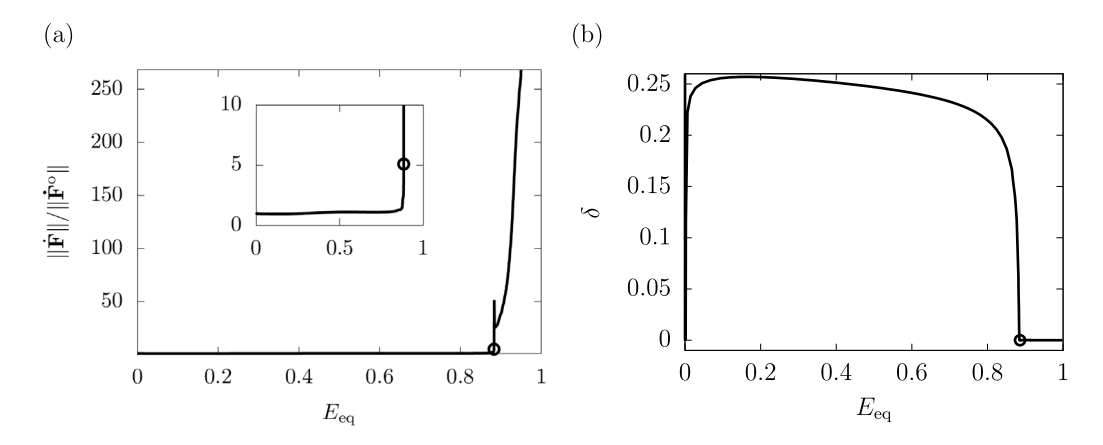


Fig. 13. (a) Localization indicator,  $\|\dot{\mathbf{F}}\|/\|\dot{\mathbf{F}}^0\|$ , entering Eq. (36) versus cell equivalent strain,  $E_{eq}$ , and (b) loss of full rankedness parameter,  $\delta$ , entering Eq. (40), versus  $E_{eq}$  for the same calculation as in Fig. 12. The onset of unhomogeneous yielding is marked with (o).

- Strain localization (•) occurs after the onset of unhomogeneous
- The energy criterion  $(\Box)$  is met but it neither corresponds to strain localization nor unhomogeneous yielding. What it physically means is therefore questionable.

It remains to assess how the surrogate localization criterion, Eq. (36), the critical strain ratio criterion, Eq. (39), and the loss of full rankedness criterion, Eq. (40), fare in comparison with the above measures. Indeed, except for Zhu et al. (2020), Cadet et al. (2022) who

used a condensation technique (Miehe, 2003) to probe the localization condition, Eq. (29), other investigators have employed Eq. (36) as a surrogate to Eq. (29); see Dæhli et al. (2022) for a more recent example.

The ratio  $\|\dot{\mathbf{F}}\|/\|\dot{\mathbf{F}}^0\|$  is plotted against the cell's equivalent strain in Fig. 15a for the cells with and without hardening. As clearly inferred from Fig. 8, deformation is not uniform on the top and bottom boundaries of the cell for the N=0.1 case. To account for this, the norm  $\|\dot{\mathbf{F}}^0\|$  is actually a surface average over the top boundary. In the literature, critical values that were used for  $\|\dot{\mathbf{F}}\|/\|\dot{\mathbf{F}}^0\|$  were much lower than those attained in the calculations. Typical values ranged

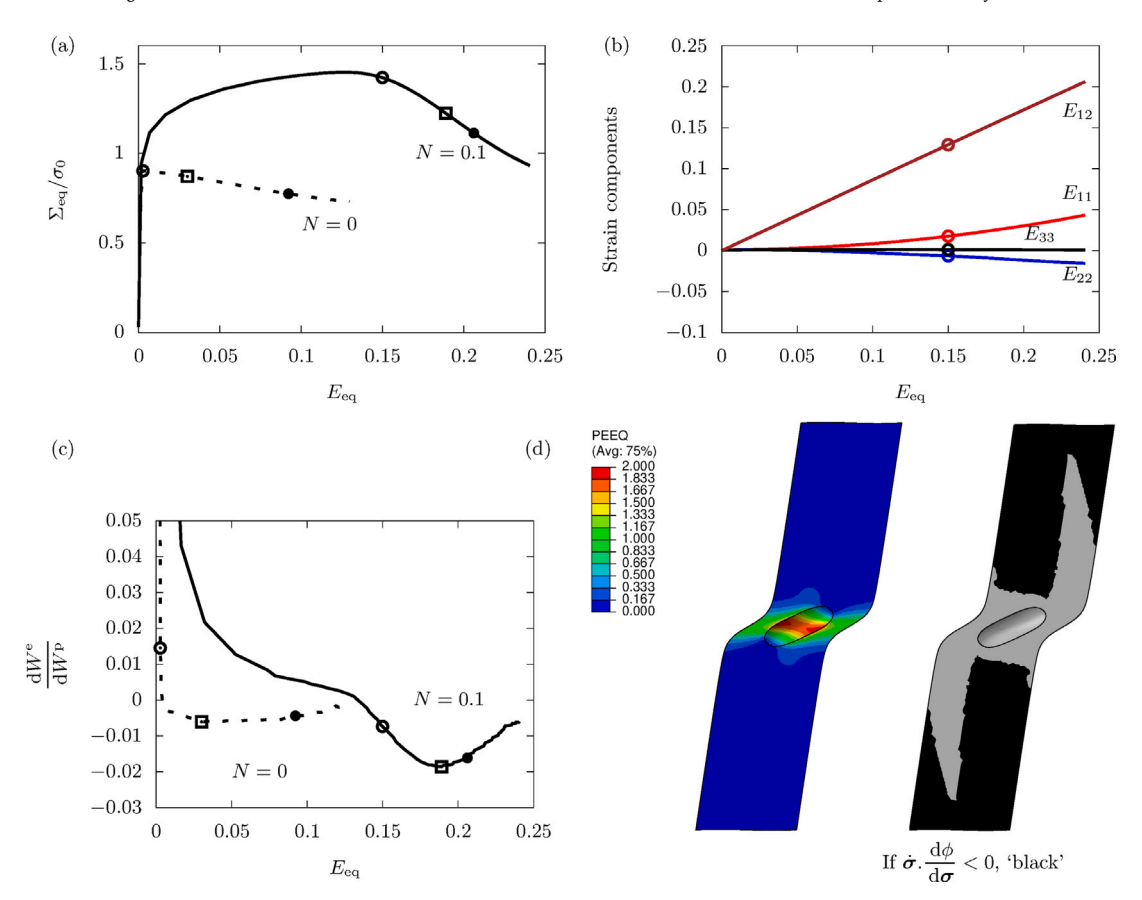


Fig. 14. (a) Overall stress–strain responses and corresponding evolution of (b) the overall logarithmic strains (N=0.1 only), and (c) the rate of change of elastic energy of the unit cell for shear loading (T=1, L=0),  $f_0=0.00353$ ,  $\lambda_0=4$  and two values of the hardening exponent N. (d) Deformed configuration at the onset of unhomogeneous yielding showing contours of effective plastic strain  $\tilde{\epsilon}$  (left) and regions of elastic unloading (painted black; right). Key: (o): onset of unhomogeneous yielding; (•): strain localization, Eq. (29); ( $\Box$ ): energy criterion, Eq. (38).

between 2 and 10. The inset in Fig. 15a shows a reduced range for the ordinate. Over that range, none of the above three criteria has yet been met. In particular, Eq. (36) which is supposed to be surrogate to the localization condition, Eq. (29), does not match the prediction of the latter. It grossly underestimates it. In fact, the surrogate criterion is closer to the onset of unhomogeneous yielding.

The criterion introduced by Tekoğlu et al. (2015), which is based on the ratio of maximum to minimum plastic strain around the void, Eq. (39), is evaluated in Appendix B. It is shown there that if the critical value Z=15 proposed by Tekoğlu et al. (2015) is used then the criterion would be met at an arbitrarily small strain.

The loss of full rankedness parameter  $\delta$ , Eq. (40), is plotted in Fig. 15b. In the non-hardening case (dashed curve), the  $\delta$  parameter decreases rapidly to zero and corresponds de facto to the onset of unhomogeneous yielding. However, it increases back again, reaches a maximum and decreases back to zero. It is checked that the determinant of  $\dot{\mathbf{F}}$  itself remains vanishingly small. So the non-monotonic behavior has to do with normalization by det  $\dot{\mathbf{F}}^{\text{ref}}$ . In the hardening case (N=0.1), the initial decrease of  $\delta$  is not as steep but occurs earlier than any other criterion. In particular,  $\dot{\mathbf{F}}$  loses full rankedness well before the onset of unhomogeneous yielding. These trends will be discussed further below.

# 3.2.3. Failure by void coalescence

From the practical point of view, the gradual decrease in the load-bearing capacity under shear loading leaves one without a simple measure of strain to failure. The situation in the absence of hardening typifies the behavior even better. To address this issue, one needs some objective definition of failure. A natural definition is when the material loses all stress carrying capacity. Since one cannot pursue the unit

cell calculations to that ultimate state we proceed by extrapolation, as indicated for making Fig. 9b. The procedure is illustrated in Fig. 16 where the overall stress–strain responses are extrapolated (linearly) to zero stress ( $\Sigma_{\rm eq}=0$ ).

As mentioned earlier, for axisymmetric tension the failure point can be identified with the onset of unhomogeneous yielding, up to a small error, Fig. 16a. However, for shear-dominant loadings, the strain to failure is much greater than either  $E_{\rm eq}^{\rm UY}$  or  $E_{\rm eq}^{\rm L}$ , Fig. 16b. The lower the hardening capacity of the matrix the greater that difference.

## 4. Discussion

The voided cell model has played a key role in the development of porous material plasticity (Tvergaard, 1982b,a, 2008, 2009). Here, three-dimensional calculations were employed under fully periodic boundary conditions to critically investigate the relative ductilities in shear and tension at fixed overall stress triaxiality. The commonly accepted trend that axisymmetric stress states are "more ductile" than shearing states was found to break down. The inverse trend of shearing states being more ductile was found for sufficiently small initial porosity, Fig. 9. In the literature, the difference between axisymmetric and shearing states, and the related effect of the Lode parameter on ductility, were only investigated for initial porosities in excess of  $f_0$  = 0.001. Here, the trend reversal is found for half that value,  $f_0 = 0.0005$ . The reversal is strictly valid in terms of an overall strain localization as a measure of ductility, Fig. 9a. If failure by (physical) void coalescence is chosen as the measure of ductility, then the trend of shearing states being more ductile is actually the norm for all cases analyzed here; see Fig. 9b.

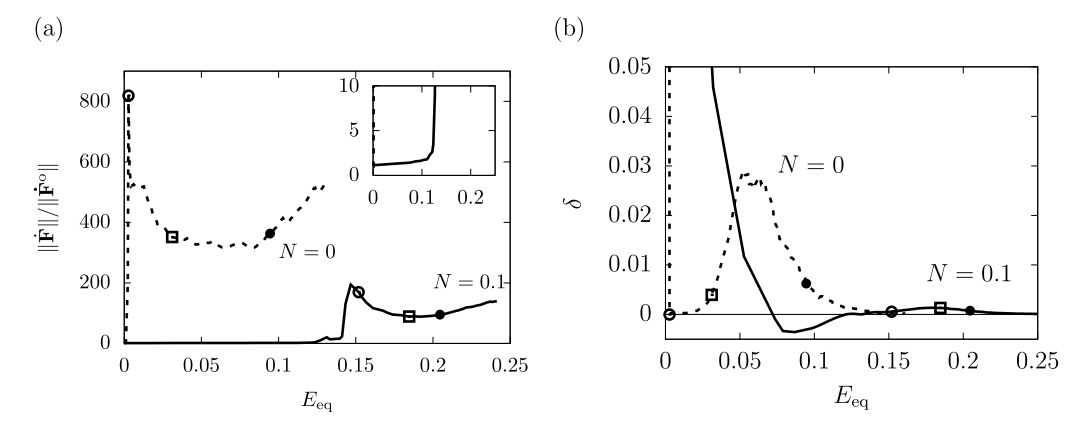


Fig. 15. (a) Localization indicator,  $\|\dot{\mathbf{F}}\|/\|\dot{\mathbf{F}}^0\|$ , entering Eq. (36) versus cell equivalent strain,  $E_{\rm eq}$ , and (b) loss of full rankedness parameter,  $\delta$ , entering Eq. (40), versus  $E_{\rm eq}$  for the same calculation as in Fig. 14. Key: (o): onset of unhomogeneous yielding; (•): strain localization, Eq. (29); ( $\square$ ): energy criterion, Eq. (38).

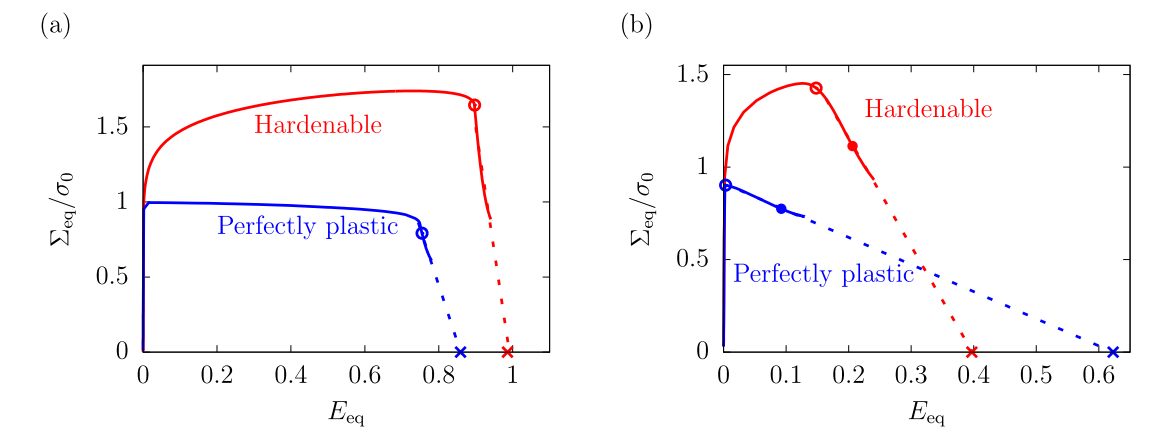


Fig. 16. Two alternative definitions of failure in the unit cell: strain localization (•) or complete loss of stress carrying capacity at void linkup by extrapolation (×). (a) Axisymmetric loading (L=-1) using  $f_0=0.001$ ,  $\lambda_0=1$ . Here,  $E_{\rm eq}^f > E_{\rm eq}^L = E_{\rm eq}^{\rm UY}$ . (b) Shear loading (L=0) using  $f_0=0.00353$ ,  $\lambda_0=4$ . Here,  $E_{\rm eq}^f > E_{\rm eq}^L > E_{\rm eq}^{\rm UY}$ .

Because of the potential implications of this finding, its dependence upon the definition of failure is paramount. To address this, we have also critically examined several criteria used by various investigators. In particular, the question of whether void coalescence occurs before or after strain localization has been discussed at length in the literature, but often based on *ad hoc* definitions.

In both English and physics, coalescence implies linkup. In the cell model, therefore, void coalescence corresponds to complete loss of load bearing capacity (the (x) in Fig. 2). If strain localization were to occur in the cell, it must set in before coalescence in the above sense. The triviality of this fact is obviously not subject to debate. What has been debated e.g. Tekoğlu et al. (2015) is the competition between strain localization and the "onset of void coalescence", defined in some way. Except for Tekoğlu et al. (2015), the onset of void coalescence in tension has been understood in the literature as the shift to a uniaxial straining mode of the cell (Pardoen and Hutchinson, 2000; Benzerga, 2002). This definition is semantically problematic because when uniaxial straining sets in, neighboring voids are still well separated and one could hardly speak of the "onset of coalescence" per se. Most importantly, the above definition is physically problematic for shearing stress states. This difficulty has led various authors to introduce new definitions of the "onset of coalescence".

Our approach has been to give up entirely on the terminology "onset of void coalescence" for any quantitative definition and adopt instead the new concept of unhomogeneous yielding, first introduced by Torki and Benzerga (2018) and further elaborated upon by Benzerga (2023). In the context of a cell (periodic or not) containing a single void, unhomogeneous yielding corresponds to a percolated state whereby the

elastically unloaded zones connect the lateral sides of the cell. This amounts to making such zones extend over a length scale comparable with the void spacing. For axisymmetric states, the onset of unhomogeneous yielding corresponds exactly to the "onset of void coalescence" in the sense of Pardoen and Hutchinson (2000), Benzerga (2002). But the concept is general enough to apply to any stress state.

An essential phenomenon that is common to both void coalescence and strain localization is elastic unloading. Yet, to date very little has been done by means of quantifying the progression of elastic unloading in the cell model. Wong and Guo (2015) attempted to introduce a measure that addresses this need. They demonstrated that a negative minimum in the cell's rate of elastic work corresponds to the onset of uniaxial straining under axisymmetric tension. Based on that, they assumed the measure to carry universal physical meaning. They and other authors used that measure in discussing void coalescence versus strain localization. There are three issues with the energy criterion of Wong and Guo (2015). First, it is only a global measure. Its simplicity is attractive but it only measures a global signature of elastic unloading. What matters for coalescence are localized elastic unloading events. Second, the existence of a negative minimum is not always guaranteed; for example if the elastically unloaded zone is not large enough (Cadet et al., 2022). Third, most practically, its physical meaning for general states is unclear. When probed against other well-defined phenomena (unhomogeneous yielding and strain localization) the energy criterion is found to correspond to neither.

When investigated in the literature, the question of void coalescence versus strain localization led to answers that seem to be greatly affected by the adopted definitions. Most studies, e.g. Barsoum and

Faleskog (2007b), Dunand and Mohr (2014), Vishwakarma and Keralavarma (2019), Dæhli et al. (2022) have used Eq. (36) as a surrogate localization criterion. However, our analysis shows that the criteria in Eqs. (29) and (36) lead to very different results with the latter being always met earlier for any reasonable value of the critical ratio in Eq. (36). This is enough to question both the validity and utility of Eq. (36) as an indicator of strain localization. Furthermore, elastic unloading is inseparable from both phenomena (void coalescence and strain localization). When it occurs, a measure such as  $\|\dot{\mathbf{F}}\|/\|\dot{\mathbf{F}}^0\|$  is bound to abruptly increase. Therefore, a criterion that sets an upper limit (e.g. 2-10) for that ratio cannot, by definition, discriminate strain localization from any other phenomenon that involves elastic unloading or even possibly strain concentration without unloading. It is therefore not surprising that Eq. (36) was found to be a better estimate of the onset of unhomogeneous yielding than of strain localization per se. As discussed by Benzerga (2023), however, unhomogeneous yielding must not be mistaken for strain localization in the sense of Rice (1976).

Another definition-dependent conclusion is that drawn by Tekoğlu et al. (2015). In addition to using a variant of Eq. (36) as a questionable criterion for strain localization, they have adopted Eq. (39) for the "onset of coalescence",3 which is also problematic. To see this, it suffices to consider a spherical void under hydrostatic loading. To the neglect of edge effects, there is no strain-rate concentration around the void because of spherical symmetry. Therefore, the ratio  $\dot{\bar{\epsilon}}_{\rm max}/\dot{\bar{\epsilon}}_{\rm min}$ remains equal to unity and the criterion is never met. This example is extreme but explains the high-triaxiality trends in Tekoğlu et al. (2015): at high values of T strain concentration around the void is weak and, depending on the value of Z, "coalescence" may nominally never be reached.4 Along the same lines, Tekoğlu et al. (2015) find that for the triaxiality investigated here (T = 1), the onset of void coalescence and strain localization are concurrent, regardless of the stress state. Again, such finding is predicated on ad hoc definitions that bear no connection to any physical phenomenon. Here, we demonstrate that the simultaneous occurrence of the two phenomena is true for axisymmetric stress states. For shearing states, however, what is meant by the "onset of void coalescence" is elusive. What we find is that strain localization occurs much beyond the onset of unhomogeneous yielding. The non-hardening case (Fig. 14) serves to demonstrate how large the "distance" between the two can be, but the finding generally holds for a hardenable matrix, Figs. 10 and 11.

Quite recently, Cadet et al. (2021, 2022) have proposed the loss of full-rankedness of the rate of the deformation gradient as a general coalescence criterion in single- or multi-void simulations. Their conclusions are, for the most part, affected by that definition. The periodicity of a single-void cell implies a single system of unhomogeneous yielding, as conceptualized in Benzerga (2023) and further illustrated through the progression of elastic unloading in the present work. It follows in that case that  $\dot{\bf F}$  is of rank 1 (opening mode) or rank 2 (sliding mode) following the terms of Benzerga (2023). Thus, unhomogeneous yielding on one system implies loss of full rankedness of  $\dot{\bf F}$ . However, the converse is not true. For example, any plane strain deformation state would lead to det  $\dot{\bf F}=0$ . This explains why the criterion was found to be satisfied early in the deformation process for the hardening case under shear; see Fig. 15b. Furthermore, if there are two or more systems of unhomogeneous yielding then  $\dot{\bf F}$  may not be singular. Thus,

the criterion proposed by Cadet et al. (2021) is neither necessary nor sufficient for unhomogeneous yielding, let alone void coalescence.

When strain localization is compared against the onset of void coalescence, it is therefore critical to probe the former using Eq. (29) directly and to define what exactly is meant by the latter. The new concept of unhomogeneous yielding helps to bring clarity into the matter and avoid the confusion that still prevails in the literature with respect to this competition. Resolving this issue has far reaching implications. Until now, the prevailing view in the literature has been that the modeling of void coalescence may be dispensed of in making estimates of what truly limits the ductility of materials. It is often argued that void coalescence modeling is still needed to simulate crack growth etc. In actuality, no estimate of ductility is reliable unless predicted using a void coalescence model, or rather a theory of unhomogeneous yielding (to employ the new terminology). As an illustration, the trend reversal uncovered by the present simulations cannot be predicted by widely used damage models that are either of the critical strain type, e.g. Bai and Wierzbicki (2010), or the shear-modified Gurson model of Nahshon and Hutchinson (2008) because both formulations have encoded the taken-for-granted fact that shearing states are always more deleterious to ductility. By way of contrast, the theory of unhomogeneous yielding makes no such assumptions a priori. It is therefore capable of predicting the "usual" trend discussed in the cell model literature (and sheet metal experimental literature) as well as the potential reversal; see e.g. Torki and Benzerga (2018), Torki (2019), Torki and Benzerga (2022).

Cell model analyses are often carried out to infer failure loci defined in terms of some measure of strain to failure versus the two loading parameters T and L. One complicating factor is the role of induced, and possibly initial, anisotropy. Thus, for fixed values of T and L, different combinations of the six overall stresses would lead to different evolutions of void and cell shapes thereby affecting the strain to failure, whatever the specific measure. A recent study by Dæhli et al. (2022) illustrates the extent of the effect, in particular when the cell is subjected to normal stresses versus when it is subjected to combined normal and shear stresses.

The method employed here to probe the localization condition, Eq. (29), is inspired from Temizer and Wriggers (2008), but is not computationally efficient. Zhu et al. (2020) have used a more efficient condensation technique (Miehe, 2003) and Cadet et al. (2022) used a variant thereof. Zhu et al. (2020) too found that the surrogate criterion, Eq. (36), is met much earlier than Eq. (29), consistent with our findings. However, they did not discuss what the discrepancy might be related to. Instead, they concluded like many others that strain localization precedes the onset of void coalescence. Again, their conclusion is based on interpreting the onset of void coalescence using the energy criterion of Wong and Guo (2015), which has been shown to lack universal validity. Likewise, the conclusions of Cadet et al. (2022) are predicated on their kinematic criterion, which has been shown to be inappropriate, in general, for coalescence or failure.

Some issues remain unresolved. First, Zhu et al. (2020) claimed that the energy criterion is always met after strain localization, probed using Eq. (29) directly. They only showed detailed results for generalized compression (L=1). Very recently, Chouksey and Keralavarma (2023) found that for plane stress states the energy criterion is met before strain localization. Our investigation shows that for L=-1 the energy criterion is concurrent with Eq. (29) but for L=0 the energy criterion is met before Eq. (29).

Second, Guo and Wong (2018) claimed that the localization condition, Eq. (29), is equivalent to an effective force in the axial spring attaining a maximum. They have not probed directly Eq. (29), but Zhu et al. (2020) did and showed that the two deliver different predictions. Interestingly, Zhu et al. (2020) did not comment on the discrepancy. The equivalence between the maximum spring force and Eq. (29) must be conditional. The difference between the maximum force criterion of Guo and Wong (2018) and Eq. (29) is reminiscent of the difference

<sup>&</sup>lt;sup>3</sup> This choice is inconsistent with Pardoen and Hutchinson (2000). Before the advent of the (also questionable) energy criterion of Wong and Guo (2015), the authors found no better way of quantitatively defining coalescence, after they defined strain localization the way they did, i.e. using a variant of Eq. (36). The reader may realize by now that the criterion they have used for strain localization is closer to the onset of unhomogeneous yielding (de facto the criterion for the onset of void coalescence in tension).

<sup>4</sup> A first-principles analysis of void coalescence shows, in fact, that high triaxiality favors early void coalescence, not the opposite.

between necking-type bifurcations and shear banding. For this reason, strain localization studies that aim at distinguishing the two probe specimens with all-around imposed displacements. That is definitely the case in the cell model. However, while overall geometric instabilities are ruled out, internal geometric instabilities cannot be. Thus, internal necking of the intervoid ligament, enabled by the presence of internal free surfaces, may explain the difference between the special localization discussed by Guo and Wong (2018) and the occurrence of a global shear band, which Eq. (29) is meant to probe.

Third, when they assessed the energy criterion, Cadet et al. (2021) made the claim that no elastic unloading occurred in their multi-void analyses. This is highly unlikely. It is possible that elastic unloading did occur locally but with no signature on the global energy measure of Wong and Guo (2015). Finally, the analyses of Cadet et al. (2022) suggest the possibility of strain localization in a void-free matrix under shear. This may be expected, at least for shearing a rigid ideal-plastic material for which the incremental equations are hyperbolic. The general implications of their observation merit study. These issues, while important, are secondary to the main subject of the paper.

The trend reversal in ductility between shearing and axisymmetric states, here mediated by the initial porosity, is independent of the critical strain measure. Ultimately, this finding has to be put to the test of experiments. In general, structural metals have no initial porosity. At nucleation, porosity levels can definitely be below the value at which the trend reversal was evidenced here. How void nucleation itself would affect the uncovered transition remains to be seen; see Noell et al. (2023) for a recent review of stress state effects on nucleation. More work is needed in this direction to make closer contact with experiments. Available experiments on sheet metal suggest a trend similar to the high-porosity regime; see e.g. Bai and Wierzbicki (2010) and references therein. However, in sheet metal whether ductility is limited by void coalescence or structural instabilities has not been carefully ascertained in the literature. Other experiments, e.g. Johnson et al. (1983), Haltom et al. (2013) show a trend consistent with the low-porosity cell predictions.

## 5. Conclusions

Unit cell calculations have been carried out for cases corresponding to axisymmetric and shearing states of loading. The two main conclusions are:

- The common belief that axisymmetric stress states are "more ductile" than shearing states was found to break down. The initial porosity content is key to modulating the relative ductility in shear versus tension.
  - Strain localization occurs earlier under shear-dominant loading than axisymmetric loading for a material with sufficiently high initial porosity. By way of contrast, strain localization occurs earlier under axisymmetric loading for a material with low initial porosity, as probably encountered in practice.
  - During unhomogeneous yielding, the rate of softening in shear is lower than in tension and the post-localization response does not exhibit a load drop. Thus, if failure is understood as the complete loss of load bearing capacity, then shearing states are more ductile than axisymmetric states irrespective of the porosity levels considered here.
- For non-axisymmetric stress states, strain localization occurs after the onset of unhomogeneous yielding regardless of strain hardening and porosity level.

### **Declaration of competing interest**

The authors declare that they have no known competing financial interests or personal relationships that could have appeared to influence the work reported in this paper.

# Data availability

Data will be made available on request

### Acknowledgments

The authors gratefully acknowledge support of this work by the National Science Foundation, United States (CMMI Award No. 1932975).

## Appendix A. Localization detection by perturbation

In elastoplasticity, the tangent operator is multi-branched. In the cell problem, this is the case at the material point level but also for the overall behavior. If the applied perturbation magnitude  $\delta F$  entering Eq. (31) is too small, one only probes the elastic branch, in which case the elastic tangent operator is too stiff and no localization is obtained. If the value of  $\delta F$  is too large, one is assured of probing the elastic-plastic branch under plastic loading, but the tangent operator may be too compliant and the strain to localization may be underestimated. Furthermore, the computed operator may be a mixture of all these parts.

To bring clarity into this, a series of preliminary analyses have been carried out by systematically varying the value of  $\delta F$  over four decades, between  $10^{-4}$  and  $10^{-8}$ , and examining the effect on the strain to localization  $E_{\rm eq}^{\rm L}$ . An example is shown in Fig. A.1. As expected,

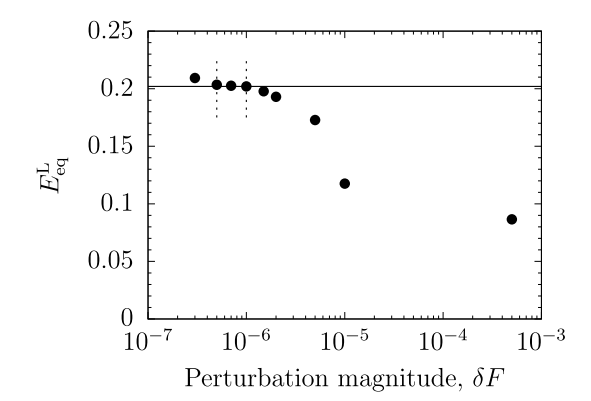


**Fig. A.1.** Strain to localization,  $E_{\rm eq}^{\rm L}$ , versus perturbation magnitude,  $\delta F$ , for shear-dominated loading (T=1,L=0),  $f_0=0.00353$ ,  $\lambda_0=4$  and N=0.1

if the perturbation is too small (e.g.  $\delta F=10^{-8}$ ) the determinant of the acoustic tensor is positive and localization is not detected. This regime is not shown in Fig. A.1. On the other hand, too large a perturbation (e.g.  $\delta F=10^{-4}$ ) leads to an early detection of localization. Interestingly, a range of values of  $\delta F$  is found where the value of  $E_{\rm eq}^{\rm L}$  is weakly sensitive to the value of  $\delta F$ . In Fig. A.1 this range is from  $5\times 10^{-7}$  to  $2\times 10^{-6}$ . Based on this and other trial-and-error analyses we have settled on the value of  $\delta F=10^{-6}$  for all analyses presented in the paper. As noted in the main text, this method is costly and very demanding on memory.

## Appendix B. Strain concentration around the void

The evolution of the ratio of maximum to minimum plastic strain around the void,  $\dot{\bar{c}}_{max}/\dot{\bar{c}}_{min}$  is shown in Fig. B.1a for the tension case

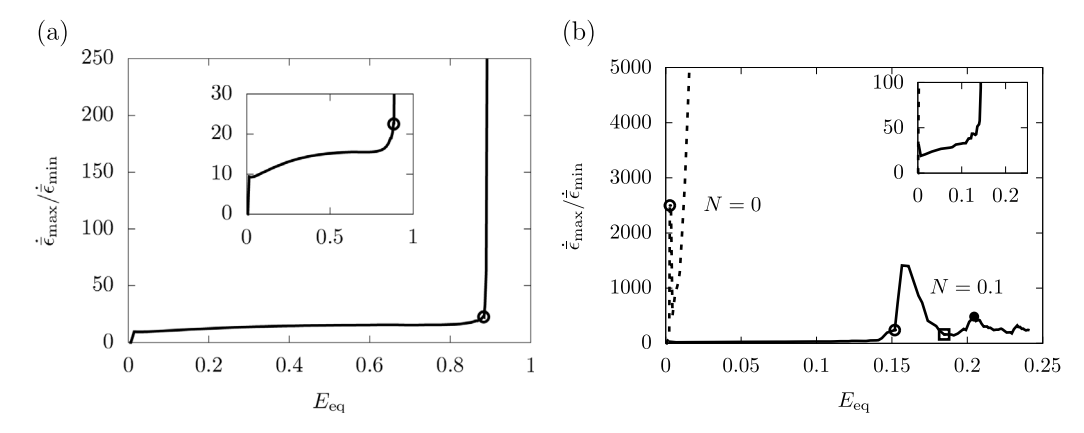


Fig. B.1.  $\dot{\epsilon}_{\max}/\dot{\epsilon}_{\min}$ , entering Eq. (39), versus  $E_{eq}$  for (a) L=-1, the same calculation as in Fig. 12, and (b) L=0, the same calculation as in Fig. 14. Key: (o): onset of unhomogeneous yielding; (•): strain localization, Eq. (29); ( $\square$ ): energy criterion, Eq. (38).

(L=-1) analyzed in Fig. 12. For this calculation, the minimum value was actually zero for much of the deformation history. Thus, what is plotted is the ratio of the strain rate averaged over twelve elements at the pole of the void to the strain rate averaged over six elements at the equator. Because the end of the curve is steep, the exact value of the critical parameter Z in Eq. (39) does not matter much for  $Z \ge 20$  or so. However, for any values below Z = 20 arbitrary values of the "coalescence strain" would be obtained; see inset in Fig. B.1a.

The same ratio is plotted against the cell's equivalent strain in Fig. B.1b for the shear case (L=0) analyzed in Fig. 14. The ratio reaches arbitrarily large values. If the critical value Z=15 proposed by Tekoğlu et al. (2015) is used then the criterion would be met at an arbitrarily small strain. If a larger critical value is used, say Z=50, then the criterion would be met close to (but before) the onset of unhomogeneous yielding. Given the corresponding levels of porosity (see Fig. 6b) one could hardly speak of void coalescence at this stage, especially for the non-hardening matrix.

## References

Bai, Y., Wierzbicki, T., 2010. Application of extended mohr–coulomb criterion to ductile fracture. Int. J. Fract. 161 (1), 1–20.

Bao, Y., Wierzbicki, T., 2004. On fracture locus in the equivalent strain and stress triaxiality space. Int. J. Mech. Sci. 46 (1), 81–98.

Barsoum, I., Faleskog, J., 2007a. Rupture mechanisms in combined tension and shear—experiments. Int. J. Solids Struct. 44 (6), 1768–1786.

Barsoum, I., Faleskog, J., 2007b. Rupture mechanisms in combined tension and shear—micromechanics. Int. J. Solids Struct. 44 (17), 5481–5498.

Barsoum, I., Faleskog, J., 2011. Micromechanical analysis on the influence of the lode parameter on void growth and coalescence. Int. J. Solids Struct. 48 (6), 925–938.

parameter on void growth and coalescence. Int. J. Solids Struct. 48 (6), 925–938. Becker, R., 2017. Direct numerical simulation of ductile spall failure. Int. J. Fract. 208, 5–26.

Benzerga, A.A., 2002. Micromechanics of coalescence in ductile fracture. J. Mech. Phys. Solids 50 (6), 1331–1362.

Benzerga, A.A., 2023. On the structure of poroplastic constitutive relations. J. Mech. Phys. Solids 178, 105344.

Benzerga, A.A., Leblond, J.-B., 2010. Ductile fracture by void growth to coalescence. In: Advances in Applied Mechanics, Volume 44. Elsevier, pp. 169–305.

Cadet, C., Besson, J., Flouriot, S., Forest, S., Kerfriden, P., Lacourt, L., de Rancourt, V., 2022. Strain localization analysis in materials containing randomly distributed voids: Competition between extension and shear failure modes. J. Mech. Phys. Solids 166, 104933.

Cadet, C., Besson, J., Flouriot, S., Forest, S., Kerfriden, P., de Rancourt, V., 2021.
Ductile fracture of materials with randomly distributed voids. Int. J. Fract. 230 (1–2), 193–223.

Chouksey, M., Keralavarma, S.M., 2023. Mesoscopic unit cell analysis of ductile failure under plane stress conditions. Int. J. Plast. 103607.

Dæhli, L.E.B., Tekoğlu, C., Morin, D., Børvik, T., Hopperstad, O.S., 2022. Ductile failure predictions using micromechanically-based computational models. J. Mech. Phys. Solids 164, 104873.

Dunand, M., Mohr, D., 2014. Effect of lode parameter on plastic flow localization after proportional loading at low stress triaxialities. J. Mech. Phys. Solids 66, 133–153.

Guo, T., Wong, W., 2018. Void-sheet analysis on macroscopic strain localization and void coalescence. J. Mech. Phys. Solids 118, 172–203. Gurson, A.L., 1977. Continuum theory of ductile rupture by void nucleation and growth:

Part i—yield criteria and flow rules for porous ductile media. J. Eng. Mater.

Technol. 99 (1), 2–15.

Haltom, S., Kyriakides, S., Ravi-Chandar, K., 2013. Ductile failure under combined shear and tension. Int. J. Solids Struct. 50 (10), 1507–1522.

Hancock, J., Mackenzie, A., 1976. On the mechanisms of ductile failure in high-strength steels subjected to multi-axial stress-states. J. Mech. Phys. Solids 24 (2–3), 147–160.

Johnson, G.R., Hoegfeldt, J., Lindholm, U., Nagy, A., 1983. Response of various metals to large torsional strains over a large range of strain rates—part 1 Ductile metals. J. Eng. Mater. Technol. 105. 42–47.

Keralavarma, S.M., 2017. A multi-surface plasticity model for ductile fracture simulations. J. Mech. Phys. Solids 103, 100–120.

Khan, I., Benzerga, A., Needleman, A., 2023. A shear modified enhanced gurson constitutive relation and implications for localization. J. Mech. Phys. Solids 171, 105153.

Koplik, J., Needleman, A., 1988. Void growth and coalescence in porous plastic solids. Int. J. Solids Struct. 24 (8), 835–853.

Leblond, J.-B., Mottet, G., 2008. A theoretical approach of strain localization within thin planar bands in porous ductile materials. C. R. Mech. 336, 176–189.

Lejeunes, S., Bourgeois, S., 2011. Une toolbox abaqus pour le calcul de propriétés effectives de milieux hétérogènes. In: 10e colloque national en calcul des structures. Clé–USB.

Miehe, C., 2003. Computational micro-to-macro transitions for discretized micro-structures of heterogeneous materials at finite strains based on the minimization of averaged incremental energy. Comput. Methods Appl. Mech. Engrg. 192 (5–6), 550–501

Miehe, C., Schröder, J., Bayreuther, C., 2002. On the homogenization analysis of composite materials based on discretized fluctuations on the micro-structure. Acta Mech. 155, 1–16.

Morin, L., Leblond, J.-B., Tvergaard, V., 2016. Application of a model of plastic porous materials including void shape effects to the prediction of ductile failure under shear-dominated loadings. J. Mech. Phys. Solids 94, 148–166.

Nahshon, K., Hutchinson, J., 2008. Modification of the gurson model for shear failure. Eur. J. Mech. A Solids 27 (1), 1–17.

Needleman, A., Tvergaard, V., 1984. An analysis of ductile rupture in notched bars. J. Mech. Phys. Solids 32 (6), 461–490.

Needleman, A., Tvergaard, V., 1992. Analyses of plastic flow localization in metals. Appl. Mech. Rev. 45, S3–S18.

Nielsen, K.L., Dahl, J., Tvergaard, V., 2012. Collapse and coalescence of spherical voids subject to intense shearing: studied in full 3d. Int. J. Fract. 177 (2), 97–108.

Noell, P.J., Sills, R.B., Benzerga, A.A., Boyce, B.L., 2023. Void nucleation during ductile rupture of metals: A review. Prog. Mater. Sci. 101085.

Pardoen, T., Hutchinson, J., 2000. An extended model for void growth and coalescence. J. Mech. Phys. Solids 48 (12), 2467–2512.

Perrin, G., Leblond, J.B., 1993. Rudnicki and Rice's analysis of strain localization revisited. J. Appl. Mech. 842–846.

Rice, J.R., 1976. Localization of Plastic Deformation. Technical Report, Brown Univ., Providence, RI (USA), Div. of Engineering.

Rudnicki, J.W., Rice, J., 1975. Conditions for the localization of deformation in pressure-sensitive dilatant materials. J. Mech. Phys. Solids 23 (6), 371–394.

Scheyvaerts, F., Onck, P., Tekoglu, C., Pardoen, T., 2011. The growth and coalescence of ellipsoidal voids in plane strain under combined shear and tension. J. Mech. Phys. Solids 59 (2), 373–397.

Tchalla, A., Belouettar, S., Makradi, A., Zahrouni, H., 2013. An abaqus toolbox for multiscale finite element computation. Composites B 52. 323–333.

Tekoglu, C., 2014. Representative volume element calculations under constant stress triaxiality, lode parameter, and shear ratio. Int. J. Solids Struct. 51 (25–26), 4544–4553.

- Tekoğlu, C., Hutchinson, J.W., Pardoen, T., 2015. On localization and void coalescence as a precursor to ductile fracture. Phil. Trans. R. Soc. A 373 (2038), 20140121.
- Tekoglu, C., Koçhan, B., 2022. Unit cell calculations under fully characterized stress states. Int. J. Plast. 156, 103358.
- Temizer, I., Wriggers, P., 2008. On the computation of the macroscopic tangent for multiscale volumetric homogenization problems. Comput. Methods Appl. Mech. Engrg. 198, 495–510.
- Torki, M., 2019. Ductile Fracture under Combined Tension and Shear: Theory and Applications (Ph.D. thesis). Texas A & M University.
- Torki, M.E., Benzerga, A.A., 2018. A mechanism of failure in shear bands. Extreme Mech. Lett. 23, 67–71.
- Torki, M.E., Benzerga, A.A., 2022. Ductile fracture in plane stress. J. Appl. Mech. 89 (1), 011001.
- Torki, M.T., Keralavarma, S.M., Benzerga, A.A., 2021. An analysis of Lode effects in ductile failure. J. Mech. Phys. Solids 153, 104468.
- Tvergaard, V., 1981. Influence of voids on shear band instabilities under plane strain conditions. Int. J. Fract. 17 (4), 389–407.
- Tvergaard, V., 1982a. Material failure by void coalescence in localized shear bands. Int. J. Solids Struct. 18 (8), 659–672.
- Tvergaard, V., 1982b. On localization in ductile materials containing spherical voids. Int. J. Fract. 18 (4), 237–252.

- Tvergaard, V., 2008. Shear deformation of voids with contact modelled by internal pressure. Int. J. Mech. Sci. 50 (10–11), 1459–1465.
- Tvergaard, V., 2009. Behaviour of voids in a shear field. Int. J. Fract. 158 (1), 41–49.
  Tvergaard, V., 2012. Effect of stress-state and spacing on voids in a shear-field. Int. J. Solids Struct. 49 (22), 3047–3054.
- Vigneshwaran, R., Benzerga, A.A., 2023. Assessment of a two-surface plasticity model for hexagonal materials. J. Magnes. Alloys http://dx.doi.org/10.1016/j.jma.2023. 04.013, In Press.
- Vishwakarma, V., Keralavarma, S.M., 2019. Micromechanical modeling and simulation of the loading path dependence of ductile failure by void growth to coalescence. Int. J. Solids Struct. 166, 135–153.
- Wong, W., Guo, T., 2015. On the energetics of tensile and shear void coalescences. J. Mech. Phys. Solids 82, 259–286.
- Xue, L., 2008. Constitutive modeling of void shearing effect in ductile fracture of porous materials. Eng. Fract. Mech. 75 (11), 3343–3366.
- Zhu, J.C., BenBettaieb, M., Abed-Meraim, F., 2020. Investigation of the competition between void coalescence and macroscopic strain localization using the periodic homogenization multiscale scheme. J. Mech. Phys. Solids 143, 104042.
- Zhu, Y., Engelhardt, M.D., Kiran, R., 2018. Combined effects of triaxiality, lode parameter and shear stress on void growth and coalescence. Eng. Fract. Mech. 199, 410–437.